Evidence for Asteroid Scattering and Distal Solar System Solids From Meteorite Paleomagnetism

James Bryson, Benjamin Weiss, Eduardo Andrade Lima, J. Gattacceca, William Cassata

The Astrophysical Journal, 892:126 (24pp), 2020 April 1 https://doi.org/10.3847/1538-4357/ab7cd4

Evidence for Asteroid Scattering and Distal Solar System Solids From Meteorite Paleomagnetism

James F. J. Bryson[1,2], Benjamin P. Weiss[2], Eduardo A. Lima[2], Jérôme Gattacceca[3], and William S. Cassata[4]
[1] Department of Earth Sciences, University of Cambridge, Downing Street, Cambridge CB2 3EQ, UK; jfjb2@cam.ac.uk
[2] Department of Earth, Atmospheric, and Planetary Sciences, Massachusetts Institute of Technology, 77 Massachusetts Avenue, Cambridge, MA 02139, USA
[3] CNRS, Aix Marseille Université, IRD, Coll France, INRA, CEREGE, Aix-en-Provence, France
[4] Lawrence Livermore National Laboratory, Livermore, CA 94550, USA
Received 2019 August 18; revised 2020 January 17; accepted 2020 March 3; published 2020 April 6

Abstract

Asteroid-sized bodies are predicted to have been scattered throughout the solar system following gravitational interactions with the giant planets. This process could have delivered water-rich small bodies to the inner solar system. However, evidence from the meteorite record supporting this scattering is limited due to difficulties in recovering the formation distance of meteorite parent bodies from laboratory measurements. Moreover, ancient millimeter-sized solids that formed in the inner solar system (calcium–aluminum-rich inclusions (CAIs) and chondrules) have also been proposed to have migrated throughout the solar system, which could have been key to their survival. Our understanding of the driving mechanisms, distances, and timings involved in this motion is also restricted for the same reasons. Here, we address these limitations by recovering the formation distance of the parent asteroid of the Tagish Lake meteorite from measurements of its natural remanent magnetization. We find that this meteorite experienced an ancient field intensity <0.15 μT. Accounting for the average effect of a tilted parent body rotation axis and possible uncertainties associated with the remanence acquisition mechanism, this result argues that the Tagish Lake parent body formed at $>$8–13 au, suggesting this body originates from the distal solar system. Tagish Lake came to Earth from the asteroid belt which, combined with our recovered formation distance, suggests that some small bodies traveled large distances throughout the solar system. Moreover, Tagish Lake contains CAIs and chondrules, indicating that these solids were capable of traveling to the distal solar system within just a few million years.

Unified Astronomy Thesaurus concepts: Meteorites (1038); Magnetic fields (994); Primordial magnetic fields (1294); Asteroid belt (70); Asteroids (72); Kuiper belt (893); Protoplanetary disks (1300); Chondrites (228); Chondrules (229); Carbonaceous chondrites (200)

1. Introduction

The orbital parameters of some Kuiper Belt objects indicate that Neptune gradually migrated outward during the first few hundred million years of the solar system. The exchange of angular momentum between Neptune and distal asteroid-sized bodies during this process caused some of these small bodies to be scattered throughout the solar system (Nesvorny 2018). Orbital evolution models propose that the gas and ice giants could have additionally scattered large numbers of asteroid-sized bodies over considerably shorter timescales ($\lesssim$0.5 Myr) during hypothesized migration events (DeMeo & Carry 2014). The first of these events (within $\sim$5 Myr of solar system formation) is Grand Tack, which involves the growth (Raymond & Izidoro 2017) and/or gas-driven migration (Walsh et al. 2011) of the giant planets. The second is the Nice model, which involves the later (likely tens of megayears after solar system formation) gas-free migration of these planets (Gomes et al. 2005). These processes have been proposed to have introduced large numbers of small bodies that formed beyond the orbit of Jupiter into the inner solar system, where a proportion could have been implanted into the asteroid belt (Levison et al. 2009). As such, small body scattering potentially played central roles in shaping the architecture of the inner solar system (DeMeo & Carry 2014), the formation of the asteroid belt (Levison et al. 2009), and the delivery of water to the inner solar system (Gomes et al. 2005). Due to difficulties in recovering quantitative constraints on the formation distances and orbital evolutions of meteorite parent bodies from laboratory measurements, direct evidence from the meteorite record supporting the migration of small bodies throughout the solar system is currently limited. However, recovered meteorite parent body formation distances that demonstrate that some of these bodies accreted in the outer solar system and subsequently traveled into the inner solar system would support this small-body motion and could provide key constraints on the roles that the giant planets potentially played in the architectural and chemical evolution of the solar system.

Constraints on the accretion distances of meteorite parent bodies could also help to elucidate the transport and survival of calcium–aluminum-rich inclusions (CAIs), the oldest solids that formed in the solar system (Scott & Krot 2014). The composition, mineralogy, and isotopic signatures of these submillimeter- to centimeter-sized refractory objects indicate that they condensed from hot nebula gas within $\sim$0.1–1.0 au of the Sun (Scott & Krot 2014), where they are then predicted to have spiraled into the Sun within 0.01–1.0 Myr (Cuzzi et al. 2003). However, CAIs comprise $\sim$0.1–4.0 vol% (Scott & Krot 2014) of the carbonaceous chondrites, a class of meteorite whose parent bodies accreted between $\sim$2.5–5.0 Myr after CAI formation (Budde et al. 2016) likely beyond the ancient orbit of Jupiter (Kruijer et al. 2017). These observations indicate that, rather than perishing quickly, some CAIs traveled large distances throughout the solar nebula, which models suggest could have been key to their survival (Ciesla 2007). Despite its

potential importance, our understanding of this outward transport is restricted because many of its key properties are poorly constrained. Four such properties are the maximum distance that CAIs traveled, the timescale of this motion, and the size and abundance of CAIs at these large heliocentric distances. Constraints on the maximum distance that CAIs traveled could be recovered from measurements of a CAI-bearing chondrite that indicate that its parent body formed in the far reaches of the solar system.

With the aim of constraining the possible distal formation of a meteorite parent body, we measured the natural remanent magnetization (NRM) carried by the Tagish Lake meteorite. Tagish Lake is a unique carbonaceous chondrite that fell on 2000 January 18 (Brown et al. 2000). Its reflectance spectrum (Hiroi et al. 2001), high H_2O, C, N, and interstellar grain concentrations (Brown et al. 2000; Grady et al. 2002; Zolensky et al. 2002), and enriched ^{15}N signature in organic nanoglobules (Nakamura-Messenger et al. 2006) have been used to argue that its parent body formed further from the Sun than those of most other meteorites (i.e., $\gtrsim$4 au, Desch et al. 2018).

Paleomagnetic measurements of individual chondrules and magnetohydrodynamical (MHD) models argue that the protoplanetary disk supported a magnetic field that likely decreased in intensity by orders of magnitude with distance from the Sun (Bai & Goodman 2009; Fu et al. 2014; Bai 2015). As such, the paleointensity experienced by a meteorite that formed within the lifetime of the disk can be used as a proxy for the formation distance of its parent asteroid. Tagish Lake was extensively aqueously altered on its parent body, which introduced a variety of secondary phases to this meteorite. One such phase is magnetite, which precipitated and grew following the reaction of pyrrhotite with aqueous fluids (Zolensky et al. 2002; Greshake et al. 2005). As such, Tagish Lake is expected to carry a grain growth chemical remanent magnetization (CRM) of any magnetic field it experienced during this alteration. The remanence carried by Tagish Lake is, therefore, analogous to that carried by the CM (Mighei-like) chondrites, which was recorded through the same process (Cournede et al. 2015).

This remanence will be a record of the solar nebula field if it was acquired within the lifetime of the nebula. The age and duration of remanence acquisition in Tagish Lake have been constrained by a number of observations. First, petrographic observations (Zolensky et al. 2002) and Mn–Cr dating of carbonates (Fujiya et al. 2013) indicate that magnetite in Tagish Lake formed at some time $\lesssim$3.8–4.1 Myr after CAI formation. The two possible age limits result from anchoring the measured $(^{53}Mn/^{55}Mn)_0$ value in these carbonates to that measured in different angrites (LEW 86010 and D'Orbigny; Fujiya et al. 2013; Doyle et al. 2015). Second, the I–Xe age of magnetite in the CI (Ivuna-like) chondrites is 2.9 $\pm$ 0.3 Myr after CAI formation (Pravdivtseva et al. 2018), indicating that magnetite was an early-forming phase during aqueous alteration of carbonaceous chondrites that share a number of similarities with Tagish Lake (e.g., carbonate formation age, Fujiya et al. 2013; magnetite morphologies and abundances, Zolensky et al. 2002; Blinova et al. 2014b; King et al. 2015; water:rock ratio, Brown et al. 2000, etc.). Third, the petrology and variation in the measured ages of secondary phases in a number of other extensively aqueously altered chondrites suggest that the entire process of aqueous alteration certainly lasted for >1 yr and much more likely lasted for ~0.1–1.0 Myr (Krot et al. 2006). Together, these observations suggest that magnetite in Tagish Lake formed some time between ~3 and 4 Myr after CAI formation, likely over a period of at least tens to hundreds of thousands of years. As such, we expect that this meteorite recorded its NRM over the same prolonged time period. The timing of nebula dissipation has also been constrained by a number of observations. The youngest time to which the nebula has been constrained to have persisted comes from the formation age of CR (Renazzo-like) chondrules (~3.7 Myr after CAI formation from Pb–Pb, Amelin et al. 2002; Al–Mg, Schrader et al. 2017; Hf–W, Budde et al. 2018, dating), which were possibly magnetized by the nebula field (Fu et al. 2019) and some of which contain nebula dust particles (Schrader et al. 2018). The oldest proposed age of nebula dissipation is ~3.8–4.8 Myr after CAI formation. This age comes from the measured formation ages of the volcanic angrites D'Orbigny and Sahara 99555 (~3.8 Myr after CAI formation from Pb–Pb dating, Tissot et al. 2017; ~4.8 Myr after CAI formation from Al–Mg, Schiller et al. 2015; Hf–W, Budde et al. 2018; Kruijer et al. 2014, dating), which experienced weak magnetic fields (<0.6 μT, Wang et al. 2017), suggesting that the nebula field had decayed and its gas and dust had dissipated around the heliocentric distance of the angrite parent body by this time. Together, all of these observations argue that it is likely that the magnetite in Tagish Lake formed within the lifetime of the nebula, such that Tagish Lake recorded a remanence of the nebula field. Moreover, the magnetite in Tagish Lake formed through the same processes (Zolensky et al. 2002), adopted similar morphologies (Hua & Buseck 1998), and was created during the same time period as that in the CM chondrites (also ~3–4 Myr after CAI formation, Fujiya et al. 2012; Cournede et al. 2015). Paleomagnetic measurements of this meteorite group demonstrate that they recorded unidirectional magnetic fields (Cournede et al. 2015). Asteroid thermal modeling indicates that the remanence acquisition age of the CM chondrites was too early for this remanence to have been imparted by an internal dynamo field created in the core of the CM parent body if this body was partially differentiated (Bryson et al. 2019). Instead, it is far more likely that the CM chondrites were magnetized by the nebula field. This observation indicates that this field persisted until at least ~3–4 Myr after CAI formation, reinforcing the argument that Tagish Lake also recorded a remanence of the nebula field. As such, the paleointensity recovered from paleomagnetic measurements of this meteorite can likely be used to constrain the formation distance of its parent body. This distance could shed light on the nature of small-body scattering and the timing and distances involved in the transport of ancient millimeter-sized solids in the protoplanetary disk.

2. Samples and Methods

2.1. Petrology of Tagish Lake

Tagish Lake is an unshocked (S1) and unweathered (W0) carbonaceous chondrite (Brown et al. 2000; Hildebrand et al. 2006). It consists of a variety of solids that accreted contemporaneously, classifying it as an accretionary breccia (Nakamura et al. 2003). It was also aqueously altered on its parent body (Zolensky et al. 2002; Greshake et al. 2005), although the persistence of some anhydrous phases (Russell et al. 2010) indicates that this alteration did not proceed to completion. However, this alteration was still extensive

throughout the matrix of this meteorite and sulphide compositions indicate that the extent of alteration was intermediate in the range observed among CM2 chondrites (Zolensky et al. 2002; Greshake et al. 2005). Tagish Lake contains rare, aqueously altered CAIs, sparse chondrules, carbonates, fine-grained aggregates, and large (hundreds of micrometers) aggregates of pyroxene, olivine, and phyllosilicates, all of which are set within an abundant fine-grained (<1 μm) matrix that consists predominately of magnetite, sulfides, and phyllosilicates (Zolensky et al. 2002; Hildebrand et al. 2006; Blinova et al. 2014a, 2014b).

The main magnetic phases that formed through parent body aqueous alteration in Tagish Lake are magnetite and pyrrhotite (Zolensky et al. 2002). This magnetite displays a range of morphologies, including framboids composed of thousands of 100–200 nm crystals (Kimura et al. 2013), stacked platelets each $\sim$1–7 μm in diameter and $\sim$0.2 μm thick (Chan et al. 2016), and single grains up to $\sim$10 μm in size (Zolensky et al. 2002; Greshake et al. 2005). The individual magnetite crystals that compose the framboids have previously been observed to adopt vortex magnetic domain structures (Kimura et al. 2013), which have recently been demonstrated to be extremely magnetically stable and are likely capable of preserving a reliable remanent magnetization for $>10^{10}$–10^{11} yr (Almeida et al. 2014; Shah et al. 2018). Pyrrhotite is found predominantly as clusters of acicular crystals $\sim$10 μm long as well as isolated crystals up to >10 μm large (Zolensky et al. 2002).

The different stones from the Tagish Lake strewn field represent different lithologies of this meteorite (Zolensky et al. 2002; Hildebrand et al. 2006; Blinova et al. 2014a, 2014b). These stones display varying degrees of aqueous alteration (Alexander et al. 2014; Blinova et al. 2014a, 2014b), leading to suggestions that the lithologies that make up Tagish Lake represent material that reached different peak metamorphic temperatures on its parent body (Alexander et al. 2014; Quirico et al. 2018). The peak temperature experienced by Tagish Lake samples 11h and 11i has previously been constrained to have been $\leqslant$ 150 °C (Herd et al. 2011), although temperatures possibly slightly higher than this value have also been suggested for these samples (Blinova et al. 2014b). We analyzed sample 10a, which reached a similar peak temperature to that of 11h and 11i (Quirico et al. 2018). It is possible that Tagish Lake could have recorded a partial thermal remanent magnetization (pTRM) during cooling from this elevated temperature. However, a pTRM recorded to $\sim$150 °C in magnetite-dominated meteorites corresponds to $\lesssim$ 2% of the total remanence (Gattacceca et al. 2016) and would be carried by grains with low blocking temperatures and coercivities whose remanence could easily have been overwritten on Earth. Additionally, a pTRM imparted to pyrrhotite or magnetite up to 150 °C is unlikely to have persisted reliably over the lifetime of the solar system (Carporzen et al. 2011). Given the small magnitude of this remanence and the ease with which the magnetization of these grains could be overprinted or lost, it is very unlikely that we would be able to recover such a pTRM recorded by Tagish Lake.

2.2. Magnetism of Extensively Aqueously Altered Chondrites

The paleomagnetic remanences carried by a number of other aqueously altered chondrites have recently been measured. The Kaba CV chondrite (Gattacceca et al. 2016) carries a low-temperature pTRM recorded during slow cooling following mild parent body metamorphism ($\leqslant$ 300 °C). The Murchison CM2 chondrite carries a CRM predominantly by magnetite, while seven other CM2 chondrites carry CRMs predominantly by pyrrhotite (Cournede et al. 2015). The magnetite in the CM2 chondrites displays similar morphologies (Hua & Buseck 1998), formed through the same parent body alteration processes (Zolensky et al. 2002) and is a similar age (Fujiya et al. 2012, 2013) to that in Tagish Lake. The remanence carried by the CM chondrites, therefore, demonstrates that meteoritic magnetite and pyrrhotite that form through aqueous alteration are capable of recording and preserving CRMs for time periods at least as long as the age of the solar system. The paleointensity recovered from the CM chondrites is 2 ± 1.5 μT (Cournede et al. 2015). Accounting for the average affect of a tilted parent body rotation axis (see Section 4.2), this paleointensity agrees with the predicted intensity of the stable component of the nebula field at the likely formation distance of the CM parent body (see Section 4.4) (Bai 2015). Depending on the nature of CRM acquisition, this process can record paleointensities that differ from the intensity of the background field (McClelland 1996). However, the broad similarity between the measured and expected paleointensities demonstrates that the process of CRM recording in extensively aqueously altered chondrites does not appear to result in paleointensities that are significantly different from the expected values. This result indicates that the remanence we measure in Tagish Lake is, therefore, likely a reliable record of the properties of the ancient magnetic fields experienced by this meteorite when it was aqueously altered.

2.3. Sample Preparation Details

We analyzed a sample of Tagish Lake that was cut from parent sample 10a (Hildebrand et al. 2006), one of the pristine stones in the collection at the University of Alberta. Our sample was cut from the parent stone using a brass saw. It was approximately lenticular in shape and about 2.5 cm $\times$ 1.5 cm $\times$ 1 cm with fusion crust partially covering one face. We defined an orientation system and cut mutually oriented subsamples using a dry wire saw inside the class $\sim$10,000 magnetically shielded room (background DC field $<$200 nT) in the Massachusetts Institute of Technology (MIT) Paleomagnetism Laboratory. We cut multiple mutually oriented subsamples between 1 and 4 mm in size along each dimension. One of the subsamples had fusion crust on one of its surfaces and the other subsamples varied in their original distance from the fusion crust between 1 and 9 mm. The distance of the center of each subsample from the fusion crust is included in Table 1.

2.4. Alternating Field Demagnetization Measurements

We measured the NRM carried by nine subsamples of Tagish Lake using alternating field (AF) demagnetization including the fusion-crusted sample. We performed these demagnetization measurements using a 2G Enterprises Superconducting Rock Magnetometer 755 housed in the magnetically shielded room in the MIT Paleomagnetism Laboratory. The magnetometer was equipped with an automated sample handling and degaussing system (Kirschvink et al. 2008). We mounted our AF subsamples to GE 124 silica glass slides with moments $<10^{-11}$ A m^2 using superglue.

We demagnetized the NRM carried by each subsample by applying alternating fields with incrementally stronger peak

Table 1
Alternating Field Demagnetization Properties of the Natural Remanent Magnetization of Our Subsamples

Subsample		Mass (mg)	Distance from Fusion Crust (mm)	NRM ($\times 10^{-9}$ A m^2)	AF Range (mT)	N[a]	MAD (°)	dANG (°)[b]	MAD > dANG?	Decl. (°)[c]	Inc (°)[d]
TL10a-1[e]	LC	29.00	1	324.90	NRM–23	46	2.3	3.7	N	181.7	−11.1
	HC				23–145	105	28.0	22.4	Y	286.9	−26.9
TL10a-2	LC	25.02	2.5	2.22	NRM–20.5	41	16.0	82.8	N	166.1	10.5
	HC				20.5–145	110	43.1	18.8	Y	54.4	−27.2
TL10a-3	LC	16.77	2	1.61	NRM–42	67	34.6	73.3	N	155.2	−18.9
	HC				42–145	84	43.8	63.9	N	60.6	30.4
TL10a-4	LC	30.53	4	1.45	NRM–9	18	28.8	58.4	N	204.9	40.8
	HC				9–145	133	41.2	28.1	Y	51.5	−13.1
TL10a-5	LC	…[f]	∼4	0.25	NRM—8.5	17	11.5	32.9	N	208.2	−44.4
	HC				8.5–145	134	44.9	75.3	N	195.0	−36.4
TL10a-7	LC	36.55	5	2.01	NRM–39	64	18.8	64.5	N	247.4	11.4
	HC				39–145	87	48.5	8.5	Y	329.2	55.7
TL10-8a	LC	…	6	0.56	NRM–9.5	19	18.4	65.2	N	189.9	47.5
	HC				9.5–145	132	40.6	5.0	Y	5.8	15.7
TL10a-8b	LC	…	6	0.81	NRM–44	69	34.8	25.8	Y	293.9	82.1
	HC				44–145	82	49.6	39.0	Y	196.1	18.2
TL10a-9	LC	10.22	5	1.23	NRM–24	48	32.9	33.6	N	122.9	84.3
	HC				24–145	103	45.4	69.0	N	104.4	65.4

Notes.
[a] N: number of points in the AF range.
[b] dANG: deviation angle.
[c] Decl.: declination.
[d] Inc: inclination.
[e] Fusion-crusted subsample.
[f] Due to the very friable nature of Tagish Lake, we chose to handle the subsamples as little as possible, so did not weigh some subsamples.

intensities between 0 and 145 mT. For each peak intensity value, we applied alternating fields along three orthogonal directions and measured the remanence remaining in the subsample after the application of each field. Following the Zijderveld–Dunlop protocol, we averaged the three values measured at each intensity to minimize the effects of gyromagnetic remanent magnetization and spurious anhysteretic remanent magnetization (ARM) (Stephenson 1993). We identified and recovered the properties of the magnetization at low coercivity (LC) and high coercivity (HC) using principal component analysis (Kirschvink 1980). After the NRM was demagnetized, we applied and subsequently demagnetized ARMs with different bias field intensities. These remanences were imparted using an alternating field with a peak intensity of 260 mT and bias fields with intensities of 50, 5, and 0.5 μT. The bias field intensity of 0.5 μT was the weakest value we could apply reliably using the ARM set up in the MIT Paleomagnetism Laboratory. Once the final ARM had been demagnetized, we applied and subsequently demagnetized a 0.4 T isothermal remanent magnetism (IRM).

Tagish Lake is expected to have recorded its primary magnetization as magnetite grew during parent body aqueous alteration in the presence of the nebula field likely over a period of tens to hundreds of thousands of years (see Section 1). Given this long time period, we were unable to reproduce an equivalent CRM-acquisition process in the laboratory in the presence of fields with known intensities and use the demagnetization of these CRMs to constrain the paleointensity of the field that imparted the NRM. Instead, we assumed that the ARMs we applied to each subsample are proxies for this CRM and we used their AF demagnetizations to constrain the range of possible paleointensities that could have imparted the CRM (Weiss et al. 2010; Weiss & Tikoo 2014; Cournede et al. 2015). To achieve this, the recording efficiency of the different remanence types needs to be quantified, which is accomplished by calculating the ratio of the magnetization gained during the acquisition of thermal remanent magnetizations (TRMs), ARMs, and CRMs in the presence of fields with the same intensities. The average of the ARM/TRM ratio previously measured from numerous magnetite-bearing samples with a range of grain sizes is 3.33 (Weiss & Tikoo 2014). This value indicates the average TRM-equivalent intensities of the ARM bias fields we applied to our subsamples were 15, 1.5, and 0.15 μT. This ratio is uncertain up to a factor of 5 (Weiss & Tikoo 2014). The value of the CRM/TRM ratio is less well constrained. Models suggest that for long alteration timescales (0.1 Myr) the value of the CRM across most of its thermal demagnetization is a factor of ∼1–2 of the TRM, although it can be as large as ∼5–10 for shorter alteration periods (10^3 s) (McClelland 1996). Given the prolonged aqueous alteration and remanence acquisition in Tagish Lake, the CRM-equivalent field intensity is likely within a factor of ∼1–2 of TRM-equivalent intensity. As such, we chose to focus on the TRM-equivalent paleointensity values as these are better

constrained and are likely similar to the CRM-equivalent values. However, we do still consider the effect of the CRM/TRM ratio value in Section 4.4.

We recovered the TRM-equivalent paleointensity of the field that imparted the NRM using ARM, B_{ARM} and IRM, B_{IRM} demagnetization methods using

$$B_{\mathrm{ARM}} = \frac{\Delta\mathrm{NRM}}{\Delta\mathrm{ARM}_{1.5}} \times \frac{B}{f'} \quad (1)$$

$$B_{\mathrm{IRM}} = \frac{\Delta\mathrm{NRM}}{\Delta\mathrm{IRM}} \times a \quad (2)$$

where ΔNRM is the change in the NRM during demagnetization over a given AF intensity range, $\Delta\mathrm{ARM}_{1.5}$ is the change in the ARM acquired with a laboratory TRM-equivalent bias field intensity of 1.5 μT over the same AF intensity range, B is the intensity of the bias field, f' is the value of ARM/TRM (3.33), ΔIRM is the change in the IRM over the same AF intensity range, and a is a calibration factor with units of field intensity (2500 μT, the average value for magnetite-bearing samples; Weiss & Tikoo 2014). We calculated B_{ARM} using the 1.5 μT TRM-equivalent bias field ARM as this bias field intensity is strong enough to impart a resolvable HC remanence to most of our subsamples (see Section 3.2) and is similar to our recovered paleointensities (see Section 3.4). However, one of our subsamples (TL10a-8b) had a notably poorer paleomagnetic fidelity than the others (see Section 3.2) and did not acquire a resolvable HC remanence following the application of the 1.5 μT TRM-equivalent bias field intensity ARM. Consequently, we calculated the paleointensity from this subsample using the ARM imparted with a TRM-equivalent bias field intensity of 15 μT:

$$B_{\mathrm{ARM}} = \frac{\Delta\mathrm{NRM}}{\Delta\mathrm{ARM}_{15}} \times \frac{B}{f'} \quad (3)$$

where $\Delta\mathrm{ARM}_{15}$ is the change in the ARM imparted with a laboratory TRM-equivalent bias field intensity of 15 μT.

We calculated the ratios of the demagnetizations in Equations (1)–(3) by fitting a linear regression to the two sets of demagnetization data. The uncertainties on the paleointensities we present are the formal 95% confidence on these slope values calculated during this fitting procedure. We calculated the magnitude of the NRM, ARM, and IRM lost relative to the first point in the demagnetization sequence (i.e., the magnitude of the NRM in the undemagnetized subsample and the magnitudes of the ARM and IRM immediately after the application of laboratory fields) rather than use vector subtraction to identify the magnetization lost in each component (Wang et al. 2017). We chose this approach because the LC components in our subsamples are weak (~1%–9% of the 15 μT TRM-equivalent bias field ARM) and the HC components form scattered clusters of points over the origin, both of which make it difficult to identify the exact value of the LC–HC transition. Furthermore, the magnitude of the point-to-point variations within these clusters is often comparable to that of the LC component such that vector subtraction results in different slopes across the HC AF range for different values of the LC–HC transition. Our adopted approach did sometimes yield slightly negative paleointensities if the remanence lost in the HC AF range decreased in magnitude (which could be due to the acquisition of spurious ARM during AF demagnetization or the scattered nature of our HC magnetization). If this is the case, the actual HC paleointensity is likely weaker than the magnitude of the value we recover.

We constrained the paleomagnetic recording fidelity of each subsample by comparing the values of the TRM-equivalent bias field intensities we used to apply an ARM to the paleointensities we recovered across the HC AF range using our ARM paleointensity method where we compared the demagnetizations of two ARMs (Bryson et al. 2017). The paleointensities in these fidelity calculations, $B_{\mathrm{fid},0.15}$ and $B_{\mathrm{fid},1.5}$, were recovered using

$$B_{\mathrm{fid},0.15} = \frac{\Delta\mathrm{ARM}_{0.15}}{\Delta\mathrm{ARM}_{1.5}} \times \frac{B}{f'} \quad (4)$$

$$B_{\mathrm{fid},1.5} = \frac{\Delta\mathrm{ARM}_{1.5}}{\Delta\mathrm{ARM}_{15}} \times \frac{B}{f'} \quad (5)$$

where $\Delta\mathrm{ARM}_{0.15}$ is the demagnetization of the ARM imparted with a laboratory TRM-equivalent bias field intensity of 0.15 μT across the HC AF range. We calculated two metrics to quantify the paleomagnetic fidelities of our subsamples (Bryson et al. 2017). The difference metric, D'_L, was calculated as

$$D'_L = \frac{B_{\mathrm{fid},L} - L}{L} \quad (6)$$

where $B_{\mathrm{fid},L}$ is the recovered paleointensity calculated using an ARM with a TRM-equivalent bias field intensity of L. The error metric, E_L, was calculated as

$$E_L = \frac{W_L}{L} \quad (7)$$

where W_L is the 95% confidence in the calculation of $B_{\mathrm{fid},L}$ originating from the error on fitting the slope of the demagnetizations of the two ARMs. A subsample with perfect paleomagnetic fidelity will produce values of $B_{\mathrm{fid},1.5}$ and $B_{\mathrm{fid},0.15}$ of precisely 1.5 μT and 0.15 μT, respectively, such that both D'_L and E_L are zero. In reality, no sample has perfect paleomagnetic fidelity, and values of $B_{\mathrm{fid},L}$ differ from the TRM-equivalent values of the ARM bias fields such that $D'_{L_{\mathrm{therm}}}$ and $E_{L_{\mathrm{therm}}}$ are not zero. However, reliable paleointensities can still be recovered from subsamples with imperfect paleomagnetic fidelity. We deemed that a subsample had a high paleomagnetic fidelity if $B_{\mathrm{fid},L}$ is within a factor of 2 of L, i.e., $-0.5 < D'_L < 1$, and $E_L < 1$ if D'_L is positive and $E_L < 0.5$ if D'_L is negative (Bryson et al. 2017). Subsamples that satisfy both high-fidelity criteria acquired resolvable HC remanences in the presence of fields with intensities at least as weak as L and, as such, are capable of providing reliable paleointensities at least as weak as L.

2.5. Thermal Demagnetization Measurements

We attempted to recover the intensity of the field experienced by Tagish Lake from thermal demagnetization measurements of three unoriented subsamples (Tl10a-unor3, Tl10a-unor4, and Tl10a-unor5) and one subsample that was mutually orientated with respect to the AF subsamples (TL 10a-6). We adopted the alternating in-field, zero-field (IZZI) Thellier–Thellier protocol (Tauxe & Staudigel 2004). We heated the subsamples from 100 °C to 500 °C in 25 °C steps, and then to 560 °C in 20 °C steps, and finally to 580 °C in

10 °C steps. We measured the NRM remaining in the subsamples as they cooled from these temperature intervals in the absence of a field and the pTRM gained as the subsamples cooled from these temperature intervals in the presence of a 3 μT field. We conducted pTRM checks between every zero-field and in-field step across the entire temperature range. We heated the subsamples in air using a ASC Scientific TD48-SC oven housed in the shielded room in the MIT Paleomagnetism Laboratory. Due to the very friable nature of Tagish Lake, we placed our subsamples inside individual 6 mm diameter quartz tubes that were ~2 cm long and packed quartz wool around them. This setup allowed us to maintain a constant subsample orientation during heating and measuring without having to handle the subsamples directly. We AF demagnetized the quartz tube and wool assemblage prior to adding the subsamples so they had moments $<1 \times 10^{-11}$ A m^2.

2.6. First-order Reversal Curve Diagram

We characterized the remanence carriers in subsample TL10a-4 by measuring a first-order reversal curve (FORC) diagram. These measurements were conducted using a Lake Shore Cryotronics PMC MicroMag 3900 series vibrating sample magnetometer at the University of Cambridge. We measured 200 FORCs with a 2.4 mT step size, 200 ms averaging time, and a saturating field of 0.5 T (total measurement time ~1.5 hr). The FORC diagrams were processed using the VARIFORC approach (Egli 2013) in the FORCinel software package (Harrison & Feinberg 2008) with a vertical ridge smoothing factor (Sc0) of 4, a horizontal smoothing factor (Sc1) of 7, a central ridge smoothing factor (Sb0) of 4, a vertical smoothing factor (Sb1) of 7, and horizontal and vertical λ values of 0.05.

2.7. I–Xe Dating

We attempted to recover the time of remanence acquisition in Tagish Lake by dating magnetite formation using I–Xe chronology. Chondrules, course-grained olivine/pyroxene aggregates, and a magnetite separate were analyzed for I–Xe chronometry in the Livermore Noble Gas Lab at Lawrence Livermore National Laboratory. A 760 mg fragment from the interior of Tagish Lake sample 10a was gently crushed in an agate mortar and pestle. Chondrules and olivine/pyroxene aggregates were hand-picked for analysis. To separate magnetite from other fine-grained silicates, several hundred milligrams of the matrix were agitated continuously for five days in 19.5N NaOH maintained at 60 °C using a Teflon-coated magnetic stir bar (Jeffery & Anders 1970). The solution was then diluted to neutral pH with Milli-Q water. The stir bar containing the magnetic fraction was removed and the remaining solution was centrifuged to recover the silicate-rich fraction. Both of these fractions were then dried in an oven at ~65 °C. The magnetite separate was removed from the stir bar using a Nd magnet covered with weighing paper.

The magnetic separate (16.4 mg), two chondrules, and the olivine/pyroxene aggregates were wrapped in Al foil and sealed in an evacuated quartz ampoule along with Shallowater enstatite (19.9 mg) as a neutron fluence monitor and age standard. The samples and standards were co-irradiated in the pool area of the Missouri University Research Reactor, where they received a total neutron fluence of $\sim 2 \times 10^{19}$ n cm^{-2} (Pravdivtseva et al. 2017).

The samples were then loaded into small metal packets made from high-purity Pt–Ir (90:10) tubes, crimped at both ends to create an encapsulating "envelope," and placed into an ultrahigh vacuum system beneath a sapphire view port. Samples were heated with a 150 W diode laser focused onto the metal envelope and coaxially aligned with an optical pyrometer (Cassata et al. 2018).

Xenon was separated from the released gas using a bare metal cryogenic trap maintained at 90 °C. The cryogenic trap was then warmed to 220 °C to release the Xe, the gas was further purified using four SAES getters (one hot and three cold), and was analyzed using a Nu Instruments Noblesse mass spectrometer equipped with six Faraday cup detectors and four ion-counting, discrete dynode multiplier detectors. Samples were analyzed statically in peak hopping mode in four steps using all four multiplier detectors. Sample analyses were interspersed with measurements of an atmospheric Xe standard to correct for spectrometer mass discrimination and intercalibrate the multiplier detectors. Analyses of extraction line blanks bracketed every one to two gas extractions. All measurements were corrected for these extraction line blanks and are reported with 1σ uncertainties. All isochron regressions were calculated using a modified version of the MATLAB® code (Thirumalai et al. 2011). Fission corrections were applied to the total ^{132}Xe abundances measured in the chondrule and olivine/pyroxene separates prior to generating I–Xe isochron diagrams, as these aliquots contained resolvable fission excesses. A two-component deconvolution of the ^{136}Xe/^{132}Xe ratio measured in each step was performed to calculate the abundances of trapped and fissiogenic ^{132}Xe, assuming trapped ^{136}Xe/^{132}Xe = 0.3294 and fissiogenic ^{136}Xe/^{132}Xe = 1.13 (Lewis 1975).

3. Results

3.1. AF Demagnetization

The results of our NRM AF demagnetization measurements are detailed in Table 1. Zijderveld diagrams (orthographic projections of the end points of the remanence vector during demagnetization onto the north–east and up–east planes) of the NRM carried by TL10a-4 and TL10a-8a are shown in Figure 1. These Zijderveld diagrams are representative of subsamples with low values of the transition between the LC and HC AF intensity ranges (8.5–42 mT depending on the subsample) and high paleomagnetic fidelity (see Section 3.2). There is no resolvable HC component in any of the subsamples that we measured such that the points in this AF range form a cluster over the origins in their Zijderveld diagrams. These clusters are due to the randomization of domains during the application of each alternating field rather than magnetometer noise (the MIT magnetometer noise is typically on the order of 10^{-12} A m^2; Wang et al. 2017). IRM acquisition curves (Figure 2) demonstrate that only 3.5% of the saturation IRM is acquired at field intensities below the LC–HC transition in TL10a-8a, indicating that there are a very large number of grains in our subsamples with the capacity to carry an HC remanence. This observation indicates that the absence of an HC remanence in our

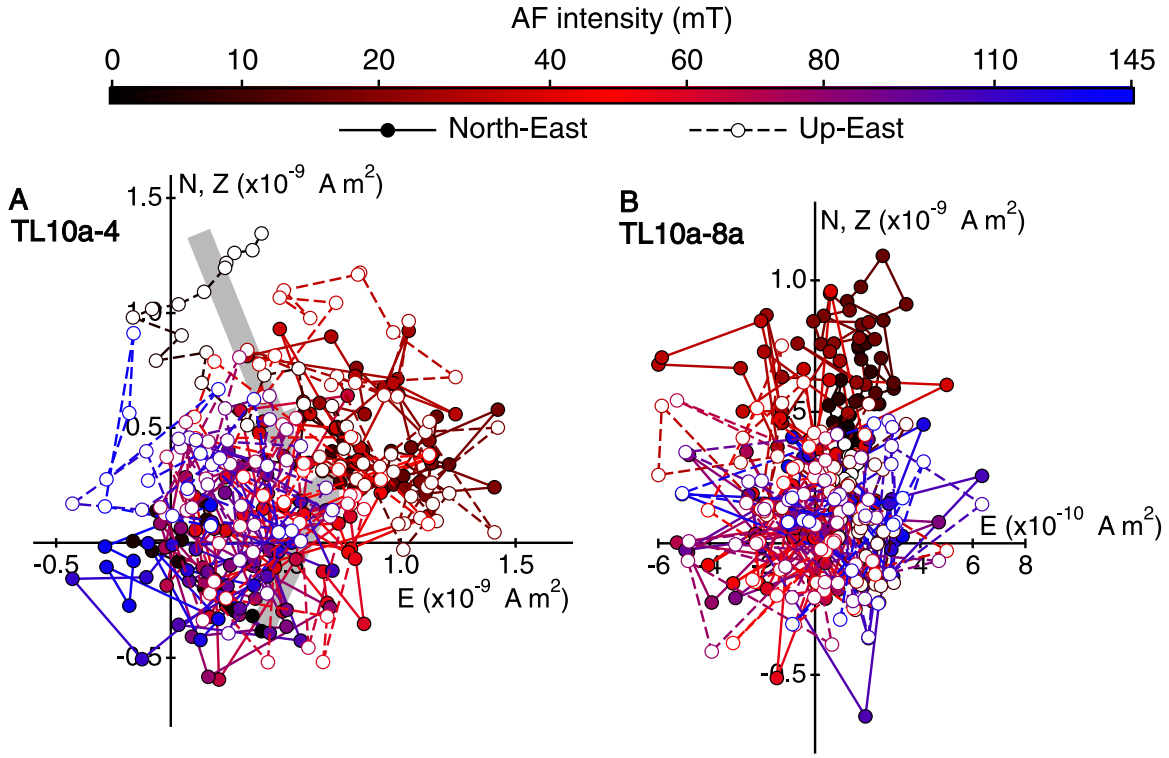

Figure 1. Orthographic projections of the end point of the natural remanent magnetization (NRM) vector onto the north–east and up–east planes (Zijderveld diagram) during NRM demagnetization of (A) TL10a-4 and (B) TL10a-8a. The intensity of the alternating field is depicted by the color of the points according to the color bar. The scatter at high coercivity is due to the randomization of domains following the application of each alternating field. The gray arrow in (A) marks the direction of the low coercivity (LC) component. The north–east gray arrow in (A) is largely hidden behind the high coercivity (HC) cluster of points. LC arrows were not included in (B) due to the very weak and largely obscured nature of the LC component. The HC magnetizations form clusters of points over the origin in both subsamples.

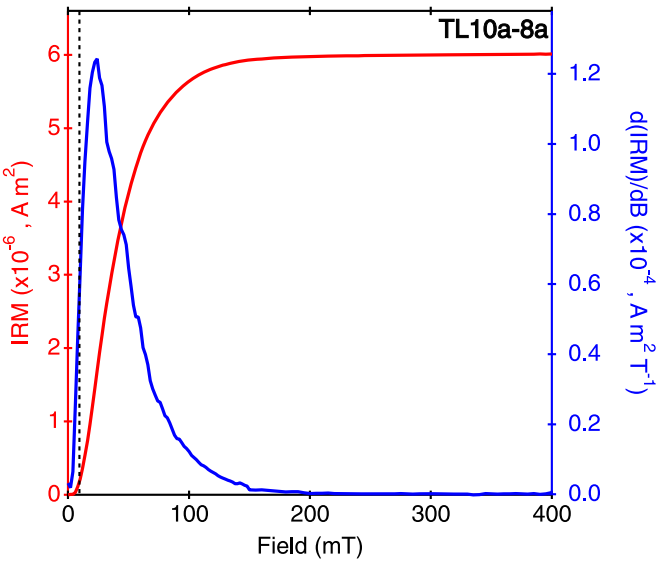

Figure 2. Isothermal remanent magnetization (IRM) acquisition (red) and coercivity spectrum (blue) of TL10-8a. The vertical dashed lines marks the LC–HC transition, which demonstrates that a very large proportion (96.5%) of the magnetic carriers in this subsample have coercivities in the HC range.

subsamples is not due to an absence of grains with coercivities in the HC range. The IRM saturates at an applied field intensity of ~225 mT.

The directions of the LC and HC components recovered from all of our AF subsamples are shown in Figure 3. The directions of the LC component in TL10a-2, TL10a-3, TL10a-4, TL10a-5, and TL10a-8a are somewhat unidirectional ($k = 3.4$; $R = 3.8$). These subsamples originate from <6 mm from the fusion crust in our parent sample (Table 1) and their LC directions are broadly similar to that of the fusion-crusted subsample (within 60°), although the LC direction of only one subsample (TL10a-3) actually overlaps with that of the fusion crust within their mean angular deviation (MAD) ellipses (Figure 3(A)) (Tauxe & Staudigel 2004). This observation hints that the LC component in these subsamples could be a pTRM resulting from heating and remagnetization in the Earth's field following atmospheric entry. However, because the LC–HC transition occurs at low AF intensities, the recovered paleointensities are much weaker than the strength of the Earth's magnetic field (see Section 3.4), and the LC component of only one subsample actually overlaps with the LC component of the fusion crust, this might only have been the case if sample 10a was tumbling quickly as it passed through the atmosphere such that a weak and only somewhat unidirectional pTRM was recorded.

The directions of the LC components recovered from subsamples that originated further from the fusion crust (TL10a-7, TL10a-8b, and TL10a-9) are up to >90° from the LC direction of the fusion-crusted subsample and are non-unidirectional (Figure 3(A)). The LC directions of TL10a-8b and TL10a-9 also have particularly large MAD values (34°.8 and 32°.9, respectively, Table 1), demonstrating that these components are not well defined. To investigate the process that could have imparted these diverse LC remanences to these subsamples, we imparted and demagnetized a viscous remanent magnetization (VRM) to TL10a-8a. We achieved this by removing this subsample from the magnetically shielded room after we had demagnetized its NRM, ARMs, and IRM so it experienced Earth's magnetic field from a demagnetized state.

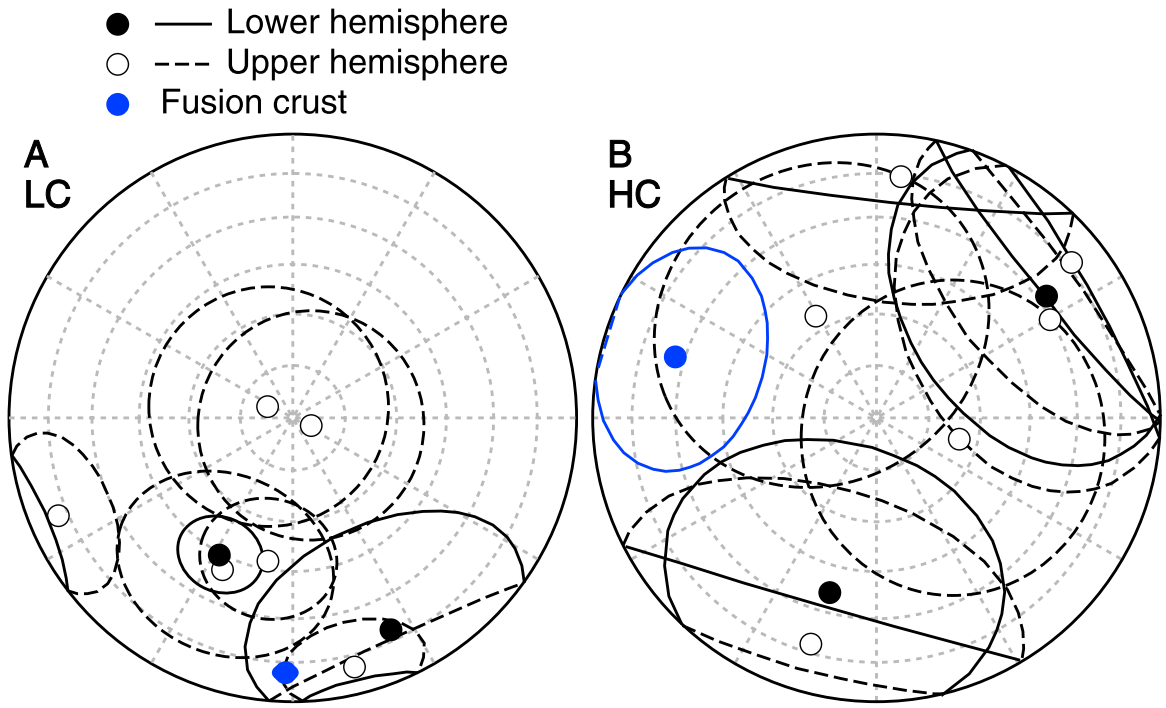

Figure 3. Equal area projections of the (A) LC and (B) HC directions of the remanent magnetization recovered from our alternating field demagnetization of Tagish Lake. The directions were calculated using principal component analysis (Kirschvink 1980). The mean angular deviation (MAD) angles are shown as ellipses. The HC directions all have large MAD angles (>40°, Table 1). The fusion crusted subsample is shown in blue.

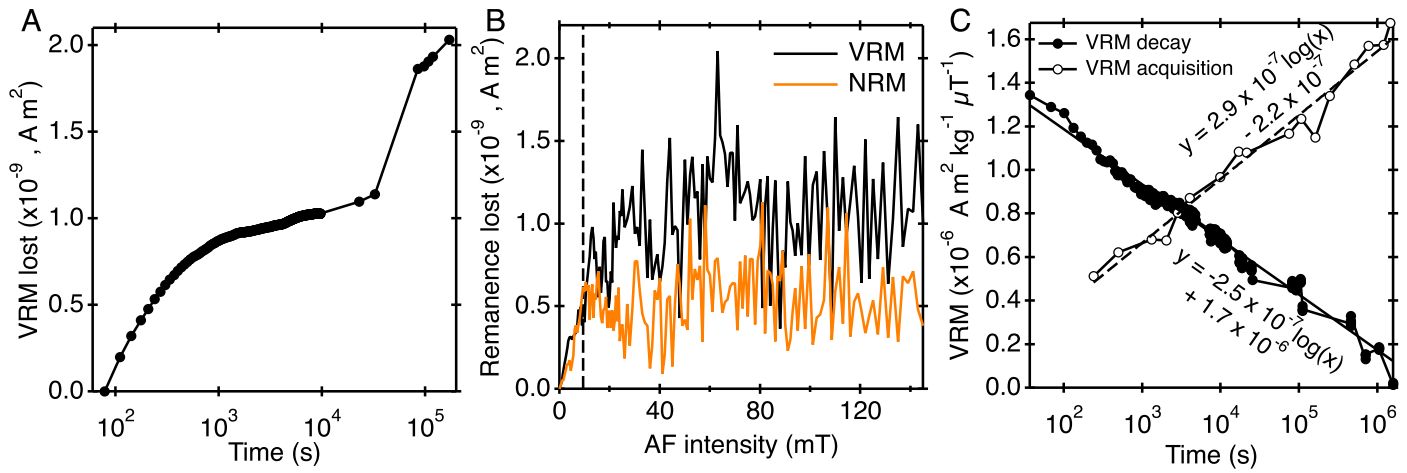

Figure 4. (A) Viscous remanent magnetization (VRM) lost over approximately two days after TL10a-8a was re-introduced to the shielded room after having experienced Earth's magnetic field for seven days. (B) VRM lost duringalternating field (AF) demagnetization immediately following the final point in (A). The VRM lost in (B) is plotted relative to the final point in (A). The magnetization lost during AF demagnetization and the value of the LC–HC transition are similar to those of the NRM. The LC–HC transition identified from the NRM demagnetization is depicted by the vertical dashed line. (C) VRM acquisition and decay over a period of ~440 hr of a 5.508 g sample of Tagish Lake. The acquisition measurements were performed in a 40 μT field.

The subsample acquired a VRM as grains with particularly low coercivity were viscously remagnetized by Earth's field. After seven days, we re-introduced the subsample to the magnetically shielded room and measured its remanent magnetization at numerous points over the next two days as the newly acquired VRM decayed (Figure 4(A)). The subsample lost $\sim 2 \times 10^{-9}$ A m^2 over this period, which is approximately a factor of 4 larger than the magnitude of the LC magnetization lost during AF demagnetization of the NRM carried by this subsample. After two days, we AF-demagnetized the remaining VRM (Figure 4(B)). The demagnetization curve of the remaining VRM is similar to that of the NRM in terms of the magnetization lost ($\sim 1 \times 10^{-9}$ A m^2) and the AF intensity of the LC–HC transition (13 mT). These similarities indicate that the LC components in TL10a-7, TL10a-8b, and TL10a-9 could be VRMs imparted by the Earth's field at low temperature that had decayed slightly during the 16 days in the shielded room before we started demagnetizing our subsamples. The parent sample we received will have changed orientations numerous times over the 17 years before we started conducting our AF-demagnetization measurements which, combined with variations in the coercivity and mineralogy of the parent sample on the millimeter length scale, will have introduced complex and multicomponent VRMs to our subsamples. The consistency between the VRM and NRM in TL10a-8a indicates that the LC remanences carried by

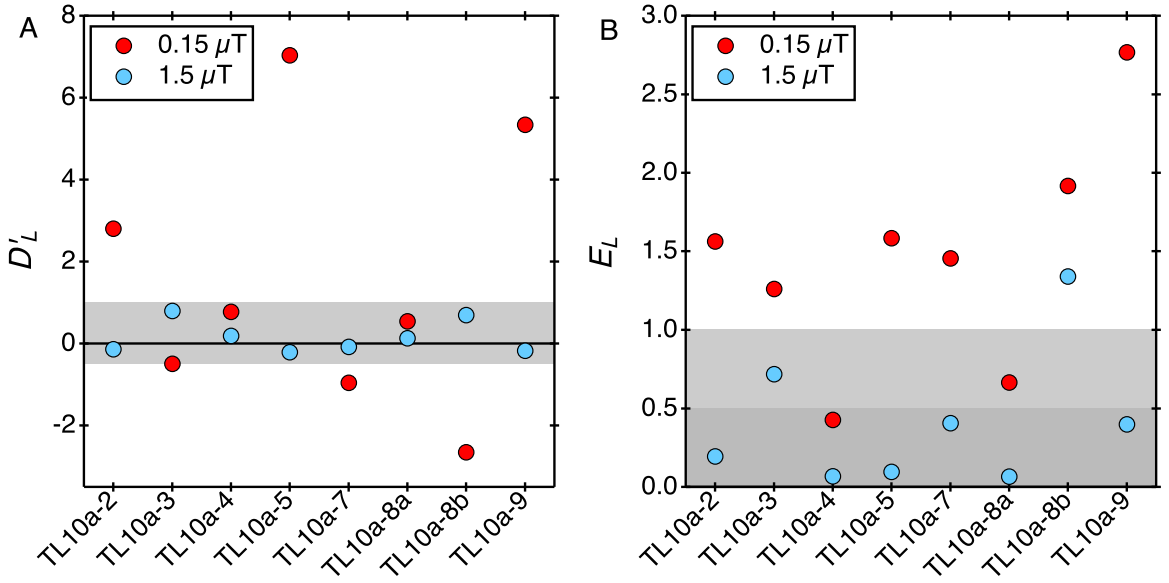

Figure 5. Values of (A) D'_L and (B) E_L for all eight nonfusion crusted AF subsamples. D'_L and E_L were calculated using Equations (6) and (7) respectively. The gray regions represent the high-fidelity ranges of these metrics. The light and dark gray regions in (B) represent high-fidelity values of E_L for positive (<1) and negative (<0.5) values of D'_L, respectively. All subsamples except TL10a-8b have both D'_L and E_L values in the high-fidelity range for the anhysteretic remanent magnetization (ARM) applied with a thermal remanent magnetization (TRM)-equivalent field intensity of 1.5 μT. Only TL10a-4 and TL10a-8a have both D'_L and E_L values in the high-fidelity range for the ARM applied with a TRM-equivalent field intensity of 0.15 μT.

TL10a-2, TL10a-3, TL10a-4, TL10a-5, and TL10a-8a could also be VRMs, and their LC directions are coincidently broadly similar to each other as well as that of the fusion-crusted sample.

We performed a second VRM experiment on a fresh undemagnetized 5.508 g piece of Tagish Lake at CEREGE (Cournede et al. 2015; Gattacceca et al. 2016). We measured the rate of VRM loss and acquisition of this sample in a 40 μT field over a period of ~440 hr (Figure 4(C)). The acquisition and loss of the VRM both vary logarithmically with time. The VRM acquisition rate is 2.94×10^{-7} A m^2 log(t)$^{-1}$ μT^{-1} kg^{-1} and the VRM decay rate is 2.54×10^{-7} A m^2 log(t)$^{-1}$ μT^{-1} kg^{-1}. These values indicate that a VRM is acquired faster than it is lost, as also observed in the CM2 chondrites (Cournede et al. 2015) and the Kaba CV3 chondrite (Gattacceca et al. 2016). Assuming a linear extrapolation of this VRM acquisition rate in log time, these values indicate that ~20%–30% of the NRM carried by this sample of Tagish Lake could have been a VRM acquired over the 18 years before we started this VRM experiment.

The HC components of the NRM across all eight non-fusion crusted subsamples are randomly oriented ($k = 1.42$; $R = 3.06$) and have large MAD values (>40°; Table 1 and Figure 3(B)). These traits demonstrate that the NRM in Tagish Lake does not contain a resolvable HC component, in agreement with the absence of a clear component in this AF range in the Zijderveld diagrams (Figure 1). These results indicate that our subsamples experienced sufficiently weak field intensities that they were not imparted with resolvable and unidirectional HC components.

3.2. Paleomagnetic Fidelity

Below a critical field intensity, the HC remanence recorded by our subsamples will be unresolvable from the AF noise resulting from the randomization of domains during the application of each alternating field. A subsample, therefore, cannot provide reliable HC paleointensities weaker than this critical field intensity. If a subsample experienced a field weaker than its critical value, the HC paleointensity value recovered using Equations (1) and (2) will be very weak and often within error of zero, which simply reflects the fact that these subsamples did not experience a field strong enough to impart a resolvable HC remanence. This critical intensity varies among our subsamples, which we constrained by calculating fidelity metrics recovered from the demagnetization of ARMs with different bias field intensities that we applied to our subsamples (Equations (6) and (7)).

The values of D'_L and E_L calculated for all of our nonfusion crusted AF subsamples are shown in Figure 5. These values calculated using $B_{\mathrm{fid},1.5}$ fall in the high-fidelity range for both metrics for all but one of our subsamples (TL10a-8b). These observations indicate that field intensities greater than 1.5 μT are required to impart resolvable and reliable remanences to TL10a-8b. These observations further indicate that field intensities at least as weak as 1.5 μT can impart resolvable HC remanences to the other subsamples and paleointensities at least as weak as 1.5 μT can be recovered reliably from these subsamples. The values of D'_L and E_L calculated from $B_{\mathrm{fid},0.15}$ fall in the high-fidelity range for both metrics for only TL10a-4 and TL10a-8a. This observation indicates that the critical field intensities required to impart resolvable HC remanences to TL10a-2, TL10a-3, TL10a-5, TL10a-7, and TL10a-9 fall somewhere between 1.5 and 0.15 μT. It also indicates that field intensities at least as weak as 0.15 μT can impart a resolvable HC remanence only to TL10a-4 and TL10a-8a and paleointensities at least as weak as 0.15 μT can be recovered reliably only from these subsamples. We were not able to constrain the critical field intensity at which these two subsamples do not acquire resolvable HC remanences because a TRM-equivalent bias field intensity of 0.15 μT was the weakest value we could apply reliably using the ARM set up at the MIT Paleomagnetism Laboratory.

In summary, TL10a-8b has low paleomagnetic fidelity (capable of acquiring a resolvable HC remanence and

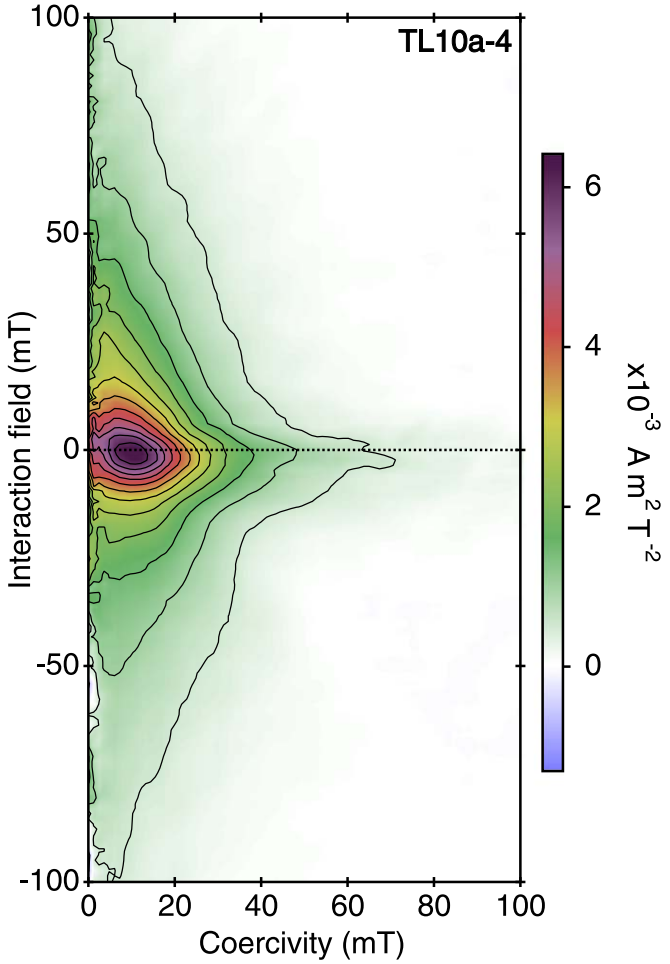

Figure 6. First-order reversal curve (FORC) diagram of TL10a-4. This diagram shows a triangular pattern. The FORC distribution contains a peak at a coercivity value of 11 mT and an interaction field value of −1 mT. This pattern matches those of magnetite powders with average grain sizes between 1.7 and 7 μm (Muxworthy & Dunlop 2002), as well as interacting, tightly packed single-domain or single-vortex grains ($\lesssim$200 nm in size) (Harrison & Lascu 2014). The contours around the peak form closed circles and are not parallel to the vertical axis, indicating that multi-domain carriers make up a small fraction of the magnetic material in this subsample.

providing reliable paleointensities for an applied field intensity somewhere greater than 1.5 μT), TL10a-2, TL10a-3, TL10a-5, TL10a-7, and TL10a-9 have intermediate paleomagnetic fidelity (capable of acquiring a resolvable HC remanence and providing reliable paleointensities for applied field intensity somewhere between 0.15 and 1.5 μT), and TL10a-4 and TL10a-8a have high paleomagnetic fidelity (capable of acquiring a resolvable HC remanence and providing reliable paleointensities for an applied field intensity somewhere less than 0.15 μT).

3.3. FORC Diagram

The FORC diagram of high-fidelity subsample TL10a-4 displays a distinctive triangular pattern that contains a peak at coercivity $B_c = 11$ mT and interaction field $B_u = -1$ mT (Figure 6). The FORC distribution extends horizontally along the coercivity axis up to $B_c \approx 100$ mT as well as vertically to $B_u \approx \pm 100$ mT at lower coercivity values. The most extreme B_u values are relatively high, so likely originate either from the crystals in the magnetite framboids that are sufficiently closely packed that they are magnetically interacting, or the nucleation of magnetic vortices in these grains, or a combination of these effects. The shape and horizontal and vertical extents of this FORC diagram are intermediate between those found in FORC diagrams of magnetite powder with average grain sizes of 1.7 and 7 μm (Muxworthy & Dunlop 2002). They are also similar to simulated FORC diagrams of interacting, tightly clustered (packing fractions >40%) magnetite grains that display single-domain and single-vortex magnetic domain states (i.e., have grain sizes <200 nm) (Harrison & Lascu 2014). FORC diagrams of single-domain pyrrhotite display an elliptical shape with a peak at a coercivity value of ~80 mT and negative interaction field values (Roberts et al. 2006). The absence of a clear signal in our FORC diagram that matches these properties demonstrates that single-domain ferromagnetic or ferrimagnetic pyrrhotite is a minor phase in TL10a-4. The contours around the peak form closed circles and the peak does not intersect the origin, indicating that multi-domain grains constitute a minor fraction of the remanence carriers in this subsample. All of these observations indicate that the predominant remanence carrier in TL10a-4 is interacting magnetite with grain sizes certainly <7 μm that display single-domain or single-vortex domain states. These grain sizes and domain states are consistent with microscopic observations of magnetite grains in Tagish Lake (Zolensky et al. 2002; Greshake et al. 2005; Kimura et al. 2013).

The hysteresis properties extracted from the FORCs are: saturation magnetization $M_s = 4.74$ A m^2 kg^{-1}; saturation remanence magnetization $M_{rs} = 0.27$ A m^2 kg^{-1}; coercivity $B_c = 5.5$ mT; coercivity of remanence $B_{cr} = 23.6$ mT.

3.4. ARM and IRM Paleointensities

The paleointensity values recovered using our ARM and IRM methods (Equations (1) and (2), Figure 7) for all of our AF subsamples across both the LC and HC AF ranges are shown in Figure 8 and are included in Table 2.

Excluding the LC paleointensities calculated from TL10a-5 that are clearly anomalous, the average LC paleointensity calculated using the ARM and IRM methods are 0.76 ± 0.45 μT and 0.67 ± 0.35 μT (95% uncertainty), respectively. The LC paleointensity values calculated using the ARM and IRM methods are within error of each other for five of our subsamples. Given the broad similarity in direction between the LC components recovered from TL10a-2, TL10a-3, TL10a-4, TL10a-5, TL10a-8a, and the direction of the fusion crusted subsample, the LC paleointensities recovered from these subsamples could correspond to the time-averaged intensity of the field experienced by these subsamples as they cooled from low temperature while possibly tumbling as they entered the atmosphere. Our VRM demagnetization measurements demonstrate that these LC paleointensities could also reflect the field that imparted a VRM to these subsamples during their 17 year residence on Earth before we conducted our measurements. Either of these conclusions are supported by the demagnetization curves of the ARMs acquired with TRM-equivalent bias field intensities of 1.5 μT. This bias field is within a factor of two of the recovered average LC paleointensity and these ARMs display significant loss of magnetization outside of the LC AF range in our subsamples (Figure 9). Assuming our ARMs are proxies for the CRM

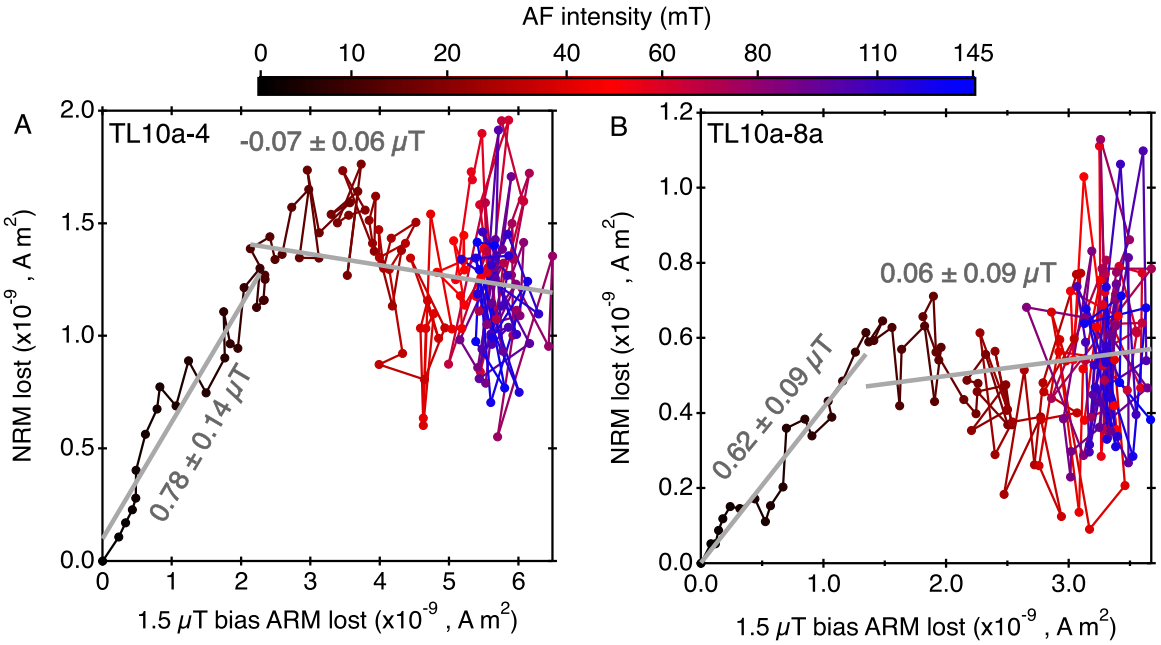

Figure 7. ARM paleointensities calculated from our high-fidelity subsamples A TL10a-4 and B TL10a-8a. The recovered paleointensities and their 95% uncertainties across the LC and HC AF ranges are included and the AF intensity of each point is depicted by the color of the point according to the color bar.

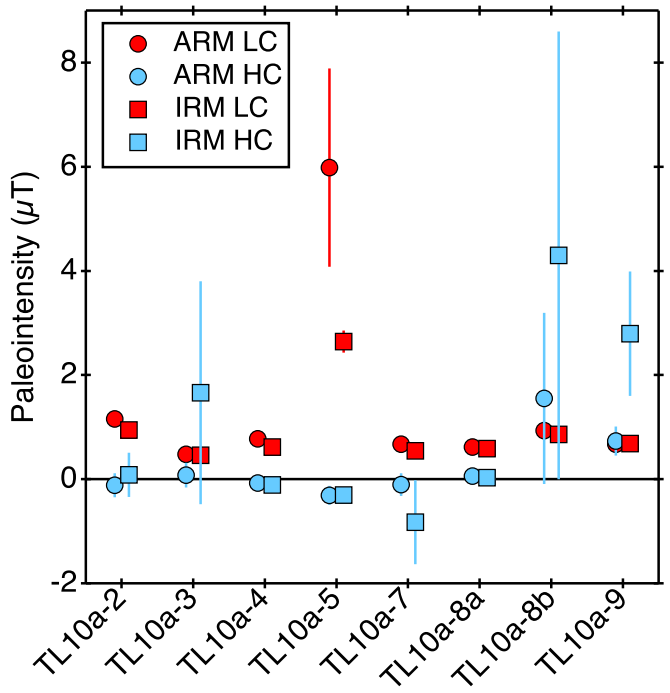

Figure 8. Paleointensities recovered across the LC and HC AF ranges using both the ARM and IRM paleointensity methods for all eight non-fusion crusted AF subsamples using Equations (1) and (2) The error bars represent the 95% uncertainty on slope fitting. The uncertainties are often smaller than the size of the points.

carried by Tagish Lake, this behavior suggests that the coercivity range that carries the LC remanences in our NRMs is narrower than that expected if the remanence was recorded when magnetite was forming during aqueous alteration on the parent body. This observation indicates that the LC remanences were imparted by a terrestrial process, such as very mild partial thermal remagnetization from atmospheric entry or viscous remagnetization, which only affects the lowest coercivity grains in a subsample.

We also calculated HC paleointensities using our ARM and IRM paleointensity methods (Equations (1) and (2)). The HC paleointensities are typically weaker than the LC paleointensities and are within error of zero for five of our subsamples using the ARM paleointensity method and four of our subsamples using the IRM paleointensity method (Figure 8 and Table 2). As discussed in Section 3.2, the critical field intensity below which TL10a-8b is incapable of providing reliable paleointensities is somewhere greater than 1.5 μT, and the critical field intensity below which TL10a-2, TL10a-3, TL10a-5, TL10a-7, and TL10a-9 are incapable of providing reliable paleointensities is somewhere between 1.5 and 0.15 μT. The recovered HC ARM paleointensities from these six subsamples are mostly <0.15 μT (within 95% confidence), which is below the minimum possible value that could be reliably recovered from any of these subsamples. This observation indicates that these subsamples experienced field intensities below their critical limits (i.e., certainly <1.5 μT). The recovered HC paleointensities in Table 2 are, therefore, not accurate estimates of the field intensity experienced by these subsamples and instead reflect the fact that they experienced paleointensities too weak to impart resolvable HC remanences. Subsamples TL10a-4 and TL10a-8a have high paleomagnetic fidelity and the critical field intensity below which these subsamples are incapable of recording resolvable HC remanences lies somewhere less than 0.15 μT. The HC ARM paleointensities recovered from these subsamples are -0.07 ± 0.06 μT and 0.06 ± 0.09 μT, respectively (Figure 7), and the recovered IRM paleointensities are -0.11 ± 0.08 μT and 0.03 ± 0.11 μT, respectively. The negative values recovered from TL10a-4 are likely due to spurious ARM acquisition during AF demagnetization due to imperfect AF waveforms and/or the scatted nature of the HC remanence. As we were unable to demonstrate that these subsamples could provide reliable estimates of such weak paleointensities, the most reliable

Table 2
Paleointensities Calculated Using Anhysteretic Remanent Magnetization and Isothermal Remanent Magnetization Techniques

Subsample		1.5 μT ARM Paleointensity (μT)	1.5 μT ARM Paleointensity 95% Uncertainty (μT)	IRM Paleointensity (μT)	IRM Paleointensity 95% Uncertainty (μT)
TL10a-2	LC	1.2	0.1	0.9	0.1
	HC	−0.1	0.2	0.1	0.4
TL10a-3	LC	0.5	0.1	0.5	0.1
	HC	0.8	0.9	1.7	2.1
TL10a-4	LC	0.8	0.1	0.6	0.1
	HC	−0.1	0.1	−0.1	0.1
TL10a-5	LC	6.0	1.9	2.6	0.2
	HC	−0.3	0.2	−0.3	0.1
TL10a-7	LC	0.7	0.1	0.5	0.04
	HC	−0.4	0.4	−0.8	0.8
TL10a-8a	LC	0.6	0.1	0.6	0.1
	HC	0.1	0.1	0.03	0.1
TL10-8b[a]	LC	0.9	0.1	0.9	0.1
	HC	1.6	1.6	4.3	4.3
TL10a-9	LC	0.7	0.1	0.7	0.1
	HC	0.7	0.3	2.8	1.2

Notes.
[a] ARM paleointensities calculated by normalizing the NRM to the ARM acquired in a TRM-equivalent bias field of 15 μT using Equation (3).

constraint we can confidently draw from these paleointensity values is that these subsamples certainly experienced TRM-equivalent ancient field intensities <0.15 μT.

Given the uncertainties in ARM and IRM paleointensity discussed in Section 2.4, we chose to also constrain the paleointensity of the field experienced by our high-fidelity samples by comparing the relative changes in their NRM and ARM demagnetizations across the HC AF range. We achieved this by normalizing the NRM and ARM demagnetization curves to their values at the LC–HC transition (Figure 9). The normalized ARM curves show large, systematic changes in normalized magnetization lost across the HC AF range. Assuming that the ARMs we applied are proxies for the CRMs recorded by Tagish Lake (see Section 2.4), we expect the normalized NRM curves to also display a resolvable change across the HC AF range if our subsamples experienced fields with intensities $\geqslant$0.15 μT. The normalized NRM demagnetization curves for these subsamples do not show a resolvable change across the HC AF range and instead show, on average, a constant normalized NRM lost value of $\sim$1 across this AF range. This difference between the normalized NRM and ARM curves indicates that these subsamples experienced ancient TRM-equivalent field intensities <0.15 μT. As a TRM-equivalent bias field intensity of 0.15 μT was the weakest value we could reliably apply, we believe that this is the most reliable paleointensity constraint we can confidently draw by comparing the relative changes in the ARM and NRM demagnetizations. This paleointensity matches that drawn from our ARM and IRM paleointensity methods from these subsamples.

3.5. Thermal Demagnetization Measurements

We performed Thellier–Thellier thermal demagnetization measurements on four subsamples. This involved measuring the magnetic remanence carried by each subsample as it cooled from multiple temperature values between 100 °C and 580 °C in the absence of a field and in the presence of a 3 μT laboratory field. Arai diagrams (NRM remaining against pTRM gained) for all four subsamples are shown in Figure 10. The absence of a clear negative or flat slope at higher temperatures in any of our Arai diagrams suggests that our Thellier–Thellier measurements were not successful. The values of the pTRM checks across the entire heating range are also large for all four subsamples (typically tens of percent with the largest being >100%), further indicating that our Thellier–Thellier measurements were unsuccessful. The Zijderveld diagrams constructed from the zero-field steps in the Thellier–Thellier measurements (Figure 11) show a loss of magnetization at lower temperatures in TL10a-6 and TL10a-unor4, which could be due either to the removal of a terrestrial overprint (VRM or pTRM acquired following atmospheric heating) or the destruction of magnetite during heating. Subsamples TL10a-unor3 and TL10a-unor5 do not show a clear low-temperature component.

To investigate the reason behind this failure, we applied a 0.4 T saturation isothermal remanent magnetization (SIRM) to the subsamples after we had heated them to 580 °C, which completely magnetized the subsamples and provided the value of the maximum possible remanent magnetization. The SIRM per unit mass of the thermally demagnetized subsamples is approximately an order of magnitude less than that of our unheated AF subsamples (Figure 12), indicating that $\sim$90% of the possible magnetization was thermochemically destroyed during heating. The altered nature of our subsamples is further supported by the very large values of the pTRM checks (Figure 10), which indicate that the magnetic make-up of the subsamples altered significantly across the entire temperature range. This alteration readily explains the failure of our measurements and the absence of a clear low-temperature component in TL10a-unor3 and TL10a-unor5. Furthermore,

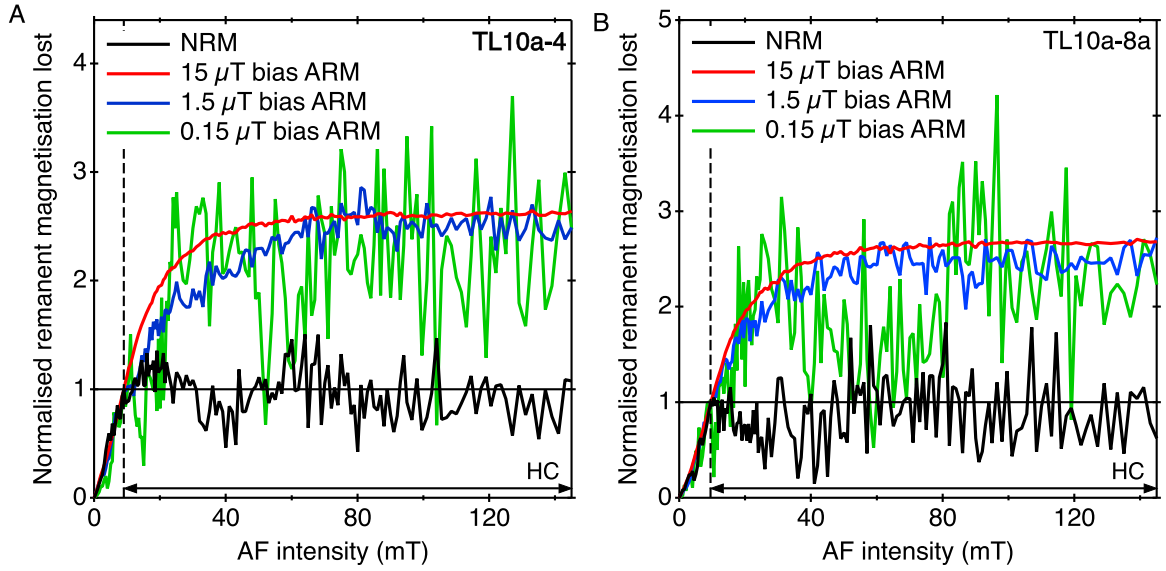

Figure 9. Normalized NRM and ARMs lost in (A) TL10a-4 and (B) TL10a-8a. The LC–HC transitions are marked by the dashed vertical lines. The curves are normalized to their magnetizations at this AF intensity. The normalized ARM demagnetization curves show pronounced differences in their shapes compared to that of the NRM curve at high coercivities (right of the dashed vertical line), which supports a paleointensity <0.15 μT.

widespread alteration means we cannot determine whether the changes in magnetization we measured during thermal demagnetization of the NRM were due to the removal of a remanence, or the destruction of magnetite, or a combination of these effects. Hence, any paleointensities calculated from these data would be inherently unreliable and meaningless. Based on all of these observations, we chose to only constrain the paleointensity experienced by Tagish Lake using our non-heating ARM and IRM techniques (Section 3.4).

3.6. Tagish Lake Magnetite Formation Age and Parent Body Accretion Age

I–Xe isochrons are shown alongside data from Shallowater enstatite in Figure 13 and complete analytical results are included in Table 3. Radiogenic ^{129}Xe (^{129}Xe*) was not observed in any of the Tagish Lake separates that we analyzed. The magnetite separate (Figures 13(A) and (B)) contains a mixture of P3, P6, and HL components (Ott 2002) that are most easily distinguished by comparing ^{136}Xe/^{132}Xe versus ^{134}Xe/^{132}Xe and ^{136}Xe/^{132}Xe versus ^{130}Xe/^{132}Xe (Table 3). These components are typically carried by pre-solar nanodiamonds (Ott 2002), which indicates that our magnetite separation procedure did not completely remove non-magnetic phases. Iodine-derived ^{128}Xe produced during neutron irradiation (^{128}Xe$_I$) was released at low extraction temperatures, indicating it may be loosely bound or surface correlated. A correlated release of ^{129}Xe* was not observed in steps containing ^{128}Xe$_I$. The olivine/pyroxene aggregates provided the most spread on an I–Xe isochron diagram, with ^{128}Xe/^{132}Xe ratios exceeding 2.5 (Figure 13(C)). The isochron appears to reflect mixing between ^{128}Xe$_I$ and adsorbed terrestrial atmospheric Xe. Like the magnetite separate, the olivine/pyroxene aggregates did not contain ^{129}Xe* correlated with ^{128}Xe$_I$. Finally, the chondrule separate did not provide spread on an I–Xe isochron diagram, although the measured ^{129}Xe/^{132}Xe ratios are consistent with trapped Xe, with no clear evidence for ^{129}Xe* (Figure 13(D)). Collectively, these observations are consistent with iodine retention/incorporation occurring at least 80 Myr after solar system formation. A similar conclusion based on comparable I–Xe analyses of magnetite in Tagish Lake was reached by a previous study (Busfield et al. 2001). Given the low-temperature history of this meteorite (Herd et al. 2011; Blinova et al. 2014b) and ancient age of its secondary minerals (Zolensky et al. 2002; Fujiya et al. 2013), it appears that iodine was mobilized by a low-temperature aqueous process that occurred without significant recrystallization of secondary minerals. Given that this I–Xe age significantly post-dates the period of early aqueous alteration on the Tagish Lake parent body (Fujiya et al. 2013), we instead recovered constraints on the timing of magnetite formation using the measured Mn–Cr ages of carbonates in Tagish Lake and I–Xe magnetite ages in the CI chondrites (Section 1).

It is possible to place broad constraints on the accretion age of a meteorite parent body from the measured ages and properties of its meteorites. For example, the time that a parent body accreted will have dictated the abundance of short-lived radionuclides (principally ^{26}Al) accreted into this body, which will have governed the amount of heating it experienced (Bryson et al. 2019). As the temperature at which aqueous alteration occurred is thought to have played a role in the nature of this process (Blinova et al. 2014b; Quirico et al. 2018), it is possible to constrain the accretion time of a parent body based on the properties of the secondary phases in its meteorites (Fujiya et al. 2012, 2013; Doyle et al. 2015). Based on the concurrent Mn–Cr ages of calcites (Fujiya et al. 2013), broadly similar nature and extent of aqueous alteration (Zolensky et al. 2002), and similar proposed water:rock ratio in Tagish Lake and the CI chondrites (Brown et al. 2000), the Tagish Lake parent body likely accreted at a similar time to that of the CI chondrites. Calculations of the thermal evolution of the CI parent body (Fujiya et al. 2013) suggest their peak metamorphic temperature and timing of aqueous alteration are consistent with the accretion of their parent body sometime between 3 and 4 Myr after CAI formation. This age is also consistent with the recent I–Xe age of magnetite in the CI chondrite Orgueil of 2.9 $\pm$ 0.3 Myr after CAI formation (Pravdivtseva et al. 2018). This observation also suggests that

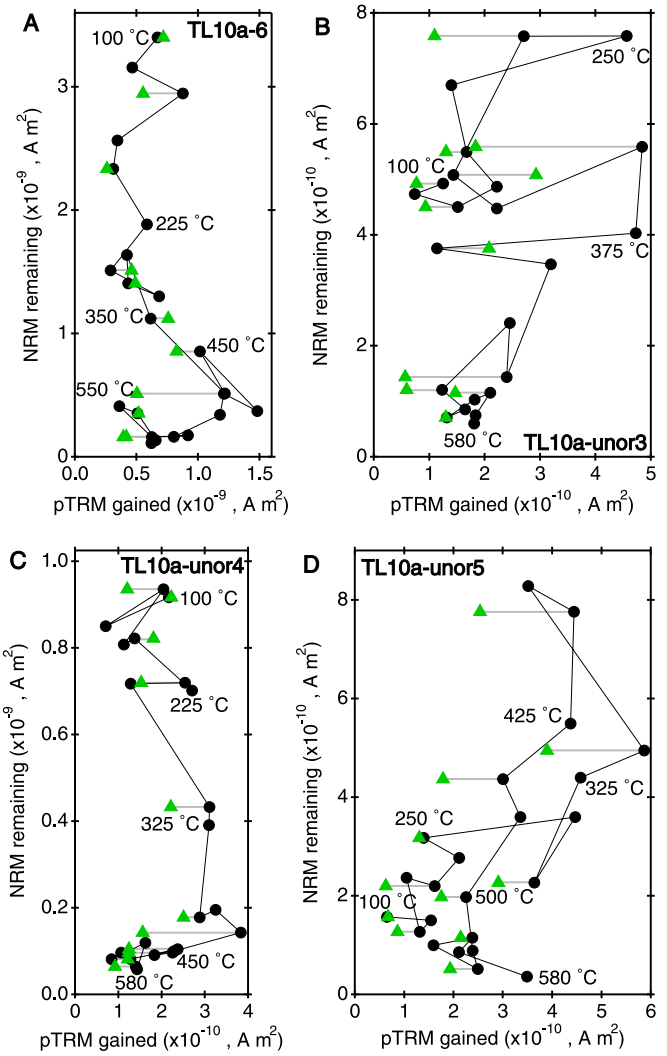

Figure 10. Arai diagrams (NRM remaining against partial thermal remanent magnetization (pTRM) gained) for all four subsamples on which we conducted Thellier–Thellier measurements. The temperatures of a handful of the points in each diagram are included. The pTRM checks are shown as green triangles. These can differ significantly (tens to hundreds of percent) from the measurements they are ideally meant to reproduce (horizontal gray lines). None of the subsamples show the negative or flat slope expected at higher temperatures expected in a successful Thellier–Thellier experiment.

magnetite formed soon after accretion in the CI chondrites. The parent body of the CM chondrites has also been proposed to have accreted within the same time period (Fujiya et al. 2012, 2013). These meteorites also underwent extensive aqueous alteration and have concurrent carbonate Mn–Cr ages with Tagish Lake and the CI chondrites (Fujiya et al. 2012) and carry a magnetic remanence consistent with the nebula field (Cournede et al. 2015), suggesting the parent bodies of extensively aqueously altered chondrites formed and underwent aqueous alteration within the lifetime of the nebula. We therefore propose that the Tagish Lake parent body likely also accreted some time between ~3–4 Myr after CAI formation, and that the magnetite in this meteorite possibly also formed very soon after accretion similar to the CI chondrites at ~3 Myr after CAI formation. This accretion age and likely magnetite formation age support Tagish Lake having recorded a remanence of the nebula magnetic field.

If the magnetite in Tagish Lake formed after the dissipation of the nebula, we would expect that this meteorite could have acquired its CRM in a very weak magnetic field environment. This would be consistent with the paleointensities we recover and would mean that we could not use this value to constrain the formation distance of the Tagish Lake parent body. However, as argued in Section 1 and throughout this section, there are a number of lines of evidence that support the magnetite in Tagish Lake having formed within the lifetime of the nebula. A final piece of evidence further supporting this early magnetite formation is the consistency with which carbonates formed between ~3–5 Myr of CAI formation across a number of different carbonaceous chondrite groups that experienced significantly different degrees of aqueous alteration and similarly low extents of thermal metamorphism (CM, CI, C2, and CR chondrites) (Fujiya et al. 2012, 2013; Doyle et al. 2015; Jilly-Rehak et al. 2017). This observation suggests that aqueous alteration in these groups (and by extension magnetite formation) was an effectively contemporaneous event, and there appear to be no weakly metamorphosed chondrites that show evidence of aqueous alteration and magnetite formation at a time when the nebula had likely dissipated (i.e., >5 Myr after CAI formation). This conclusion supports the early acquisition of a CRM in all of these groups, likely within the lifetime of the nebula. The timing of aqueous alteration (dated through fayalite formation) appears to have been slightly later in mildly metamorphosed carbonaceous chondrites (CV and CO chondrites, ~4–6 Myr after CAI formation; Doyle et al. 2015). The paleomagnetic remanence of the Kaba CV3 chondrite indicates that the magnetite in this meteorite formed in the presence of a very weak magnetic field (<0.3 μT). Coupled with the likely formation of the CV chondrite parent body shortly beyond the orbit of Jupiter (Kruijer et al. 2017; Desch et al. 2018), this weak paleointensity argues that the magnetite in Kaba did not form within the lifetime of the nebula (Gattacceca et al. 2016). The relatively late aqueous alteration experienced by these meteorites could possibly have been a consequence of the more extensive metamorphism they experienced on their parent bodies (Doyle et al. 2015). As such, it is feasible that some carbonaceous chondrites recorded aqueous CRMs after the nebula had dissipated. However, in the case of Tagish Lake (and other aqueously altered chondrites that experienced low degrees of thermal metamorphism), this process appears to have occurred within the lifetime of the nebula, such that we expect these meteorites can have recorded a vestige of this field.

4. Discussion

4.1. The Nature of the Field Recorded by Tagish Lake

The likely age of aqueous alteration in Tagish Lake (Sections 1 and 3.6) suggests that this meteorite recorded a magnetic remanence within the lifetime of the nebula, indicating that we expect it could have recorded a vestige of the field supported by the nebula. This field has been proposed to have played key roles in solar accretion and angular momentum transport in the protoplanetary disk. MHD models of the nebula predict this field consisted of an intense component, which changed direction on a ~100–1000 yr timescale (Bai & Goodman 2009), and a weak, steady vertical component with a possible contribution from a steady toroidal component, which could have been directionally constant

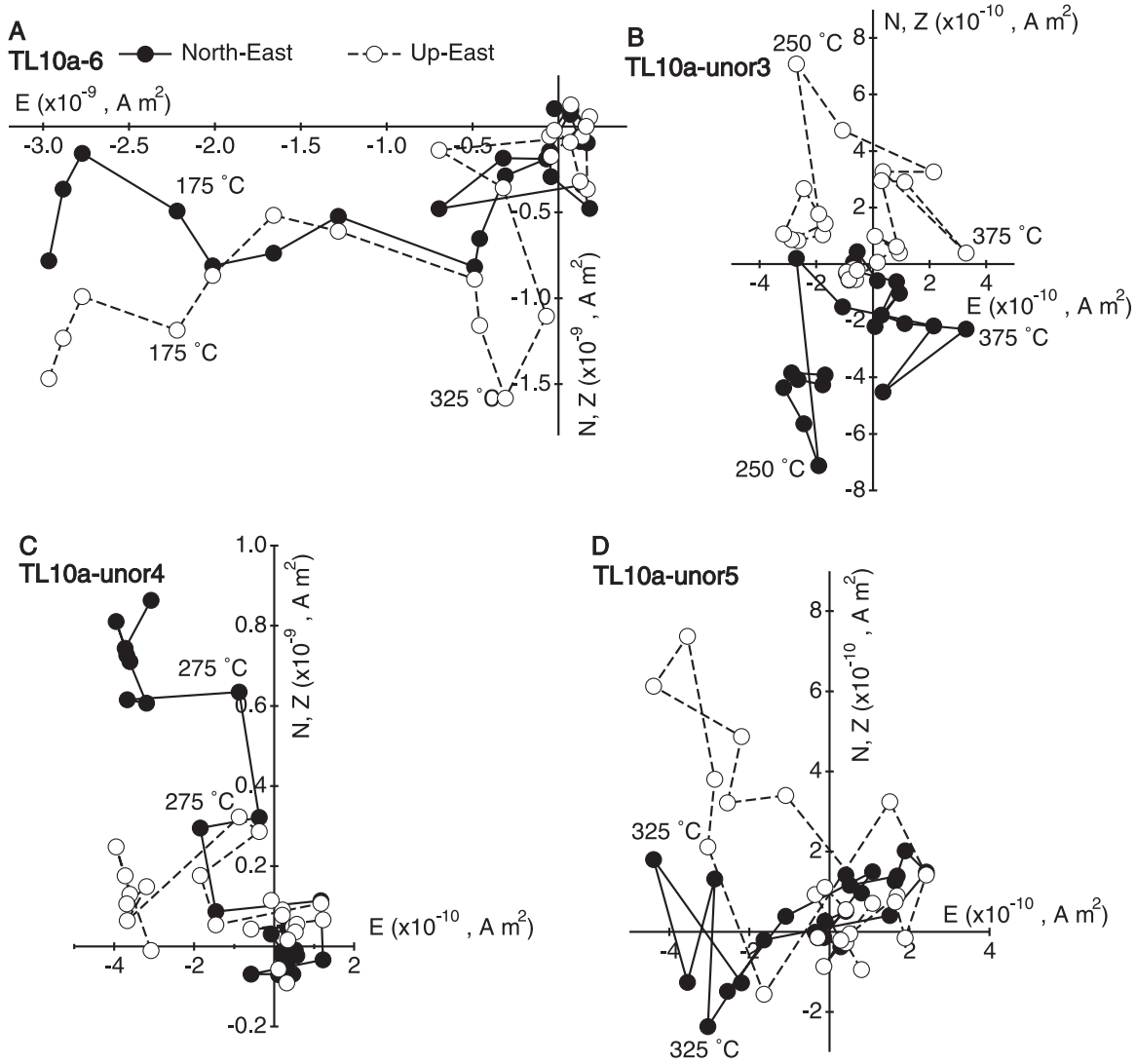

Figure 11. Zijderveld diagrams constructed form the zero-field Thellier–Thellier steps from all four subsamples that we thermally demagnetized. TL10a-6 and TL10a-unor4 display low-temperature components that could result from the loss of a terrestrial overprint, or the destruction of magnetite during heating, or a combination of these effects. TL10a-unor3 and TL10a-unor5 do not show a clear low-temperature component. None of the subsamples show a clear high-temperature component.

across the lifetime of the disk (Bai 2015). The intensity profiles of both of these components are predicted to decrease with distance from the Sun (Bai & Goodman 2009; Bai 2015). The relatively long timescale of aqueous alteration and remanence acquisition in Tagish Lake means we expect it recorded a time-averaged remanence of both components. As the timescale of variation of the intense component is much shorter than the period of remanence acquisition, we expect that the intensity of this component would have averaged to a near-zero value. On the other hand, the directional stability of the steady component means it could have imparted a unidirectional remanence to Tagish Lake across its remanence acquisition period. The prolonged remanence acquisition of this meteorite also means any short-lived spikes or other such variations in the nebula field intensity are unlikely to have imparted a recoverable remanence to Tagish Lake.

The CM chondrites also recorded a CRM as they underwent aqueous alteration at a very similar time to Tagish Lake (Sections 1 and 3.6; Cournede et al. 2015). Thus, the remanences carried by this group and Tagish lake are analogous and, as such, share very similar recording efficiencies and associated uncertainties. Accounting for the average effect of a tilted rotation axis (Section 4.2), the paleointensity recovered from the CM chondrites is 4 ± 3 μT, which agrees with model predictions of the intensity of the stable component of the nebula field at the likely formation distance of the CM chondrite parent body (Section 4.4). As discussed in Section 1, it is very likely that this remanence was imparted by the nebula field. These results, therefore, demonstrate that chondrites are capable of recording a CRM during extensive aqueous alteration, that this remanence can be a record of the stable component of the nebula field, that this remanence can persist for the lifetime of the solar system, and that the mechanism and efficiency of CRM acquisition in these meteorites do not cause paleointensities that are significantly different from the expected value to be recorded. This last observation suggests a likely value of CRM/TRM $\approx$1 during this process. All of these observations suggest that the paleointensity we recover from Tagish Lake is a reliable measure of the ancient properties of the nebula field at the formation distance of its parent body. Furthermore, the paleointensity we recover from Tagish Lake is at least an order of magnitude weaker than that recovered from the CM chondrites. As MHD models predict the nebula field intensity decreased with distance from the Sun (Bai 2015), this difference in paleointensities immediately suggests that the Tagish

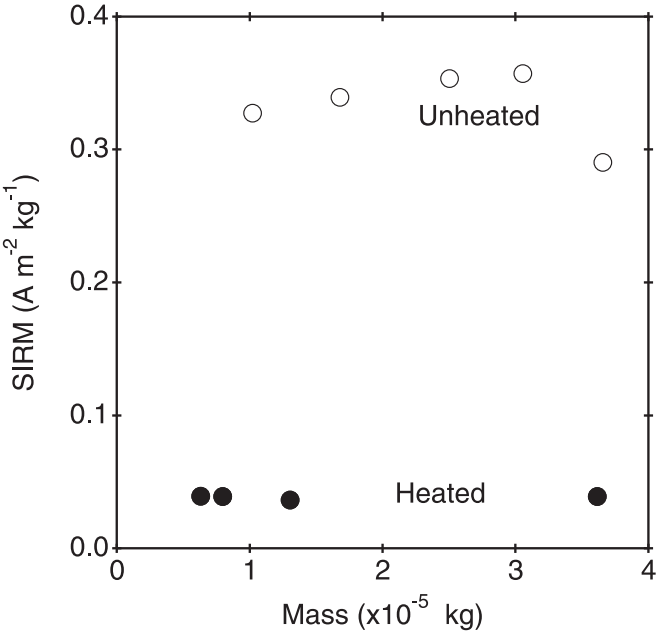

Figure 12. Saturation isothermal remanent magnetization (SIRM) per unit mass of unheated subsamples (open points) and subsamples heated to 580 °C (filled points). The SIRM for the heated subsamples is ~10% that of the unheated subsamples.

Lake parent body accreted at a larger heliocentric distance than the CM chondrite parent body. Because the remanence acquisition mechanisms in the CM chondrites and Tagish Lake are analogous and share very similar recording efficiencies, the paleointensity recovered from the CM chondrites can also be used as a reference value to allow a quantitative estimate of the formation distance of the Tagish Lake parent body to be gleaned from its recovered paleointensity limit (Section 4.4).

4.2. The Effects of the Rotation of the Tagish Lake Parent Body on the Recovered Paleointensity

The Tagish Lake parent body was likely rotating during the period that Tagish Lake recorded its NRM. As such, Tagish Lake will have experienced the time-averaged projection of the stable component of the nebula field onto the rotation axis of its parent body. This field component was orientated perpendicularly to the plane of the protoplanetary disk (Bai 2015), so the tilt angle of this rotation axis toward this plane will have dictated the time-average intensity experienced by Tagish Lake. This projected intensity varied from the intensity of the stable nebula field at a tilt angle of 0° to 0 μT at a tilt angle of 90°. Unfortunately, the tilt angle of the Tagish Lake parent body is unknown, so we could not correct the paleointensity we recovered by the precise factor to obtain the intensity of the stable component of the nebula field outside of the Tagish Lake parent body. Instead, we correct our recovered paleointensity by a factor of 2, which is the average value by which this projection factor reduces the intensity of the nebula field assuming the rotation axis could have been randomly distributed over the surface of a hemisphere (corresponding to an average tilt angle of 60°) (Fu et al. 2014). This correction factor indicates that the background nebula field at the location of the Tagish Lake parent body was most likely <0.3 μT. However, the measured distribution of present-day asteroid rotation axis tilt angles shows that only 3.6% of asteroids have tilt angles >82° and ~40% of asteroids have tilt axes <45° (Pravec et al. 2002). This observation favors a low ancient tilt angle of the Tagish Lake parent body, suggesting our adopted correction factor value of 2 is likely an overestimate. As we are only able to recover a upper limit of the field intensity experienced by Tagish Lake and a corresponding lower limit on the formation distance of the Tagish Lake parent body, we chose to still adopt a correction factor of 2 because the range of possible formation distances recovered using this value includes those recovered using smaller correction factors.

A tilted rotation axis reduces the intensity of the time-averaged field within a body. Hence, one possible explanation for the weak remanence we measured in Tagish Lake is that its parent body formed around the heliocentric distance of most other meteorite parent bodies with a high tilt angle such that the time-averaged projected field intensity experienced by Tagish Lake was <0.15 μT. As discussed in Section 4.1, the intensity of the stable component of the nebula field at the location of the CM meteorite parent body at ~3–4 Myr after CAI formation was 4 ± 3 μT (Cournede et al. 2015). Adopting a nominal value of 4 μT for the intensity of the stable component of the nebula field around the heliocentric distance of most other meteorite parent bodies at the time that Tagish Lake was aqueously altered implies that the Tagish Lake parent body had to be tilted by >87.°9 for this meteorite to have experienced a time-averaged field intensity <0.15 μT. Assuming that the rotation axis could have been randomly distributed over the surface of a hemisphere, the chance that it was tilted by >87.°9 is only 3.8%. The measured distribution of present-day asteroid rotation axis tilt angles indicates that most asteroids have low tilt angles (Pravec et al. 2002), reducing the likelihood of such a high tilt angle even further. Therefore, it is extremely unlikely that the weak paleointensity we recover from Tagish Lake is the result of a large tilt of its parent body's rotation axis.

Another possible explanation for the weak remanence in Tagish Lake is an origin around the heliocentric distance of most other meteorite parent bodies and a precessing or tumbling parent body rotation axis such that the time-averaged magnetic field experienced by Tagish Lake across its NRM recording period was very weak. It is possible that asteroid-sized bodies can precess following an impact. However, very specific relative radii of the two bodies involved in this impact are required for the necessary amount of angular momentum to be delivered to the target body for this to occur and the vast majority of these collisions are expected to cause the target body to be catastrophically destroyed. Additionally, internal dissipation causes the spin and angular momentum vectors in small bodies to align over short timescales (typically on the order of thousands of years; Burns et al. 1973). Consequently, precessing or tumbling asteroids are rare. Below we outline the precession angle we expect following a collision between two asteroid-sized bodies with various radii and the likelihood that a given collision causes the catastrophic destruction of the target body.

Following Henych & Pravec (2013), we calculated the precession angle, θ, resulting from an impact between bodies with a suite of impactor, R_I, and target, R_T, radii (Figure 14) using

$$\cos\theta = \left(1 + \frac{\sin^2\psi}{\left(\frac{L_T}{L_{\rm orb}} + \cos\psi\right)^2}\right)^{-1/2} \quad (8)$$

where L_T and $L_{\rm orb}$ are the rotational angular momentum of the target and impactor, respectively, and ψ is the angle between

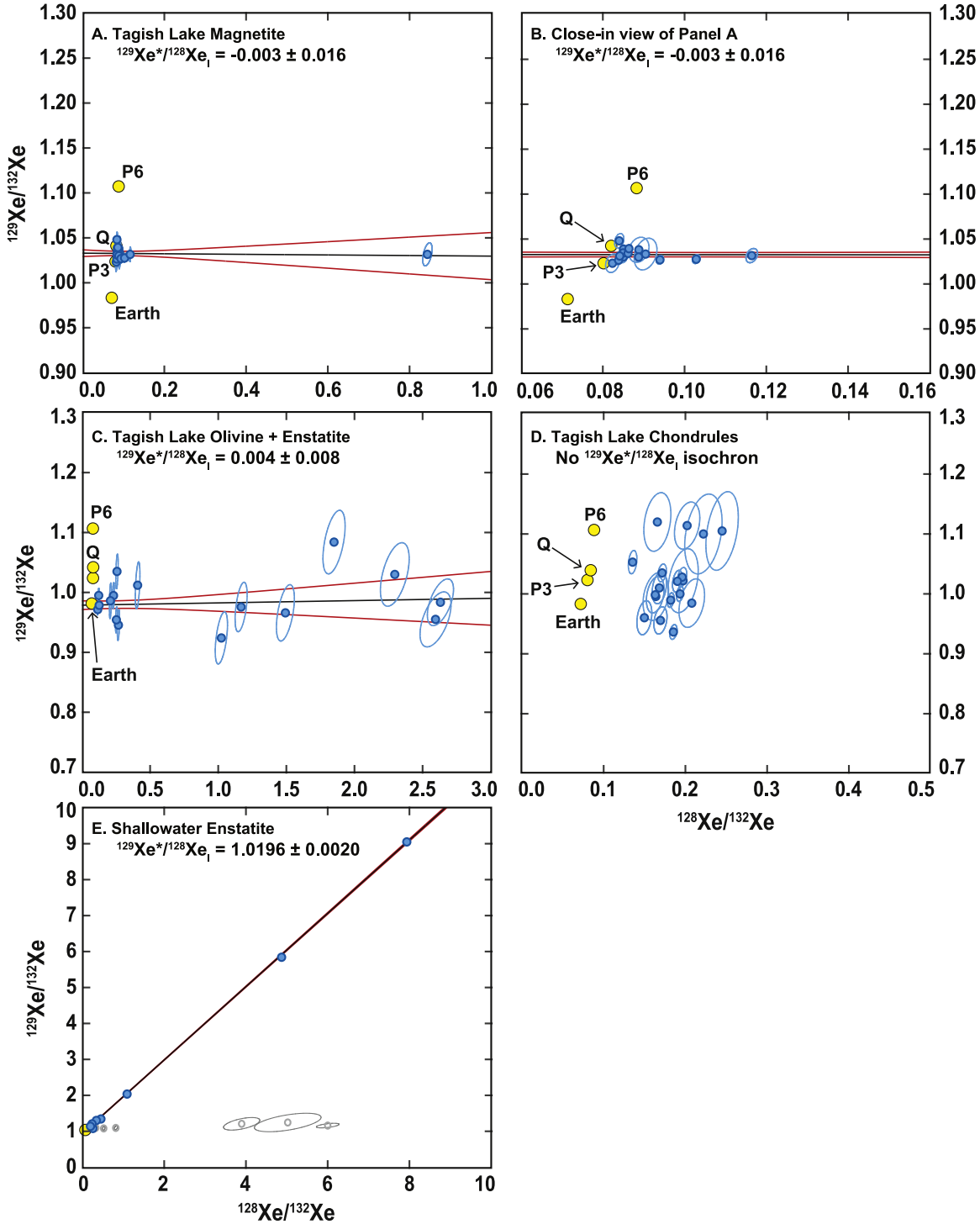

Figure 13. I–Xe isochron diagrams for (A, B) Tagish Lake magnetite, (C) Tagish Lake olivine and enstatite, (D) Tagish Lake chondrules, and (E) Shallowater enstatite. Data shown in blue were included in isochron regressions. Data shown in gray were excluded from isochron regressions. Yellow symbols denote the isotopic compositions of trapped components. Error ellipses reflect the uncertainty correlation and $\pm 1\sigma$ analytical uncertainties. The confidence intervals on the isochron regressions (red lines) are shown at 1 standard error, and the slopes ($^{129}Xe^*/^{128}Xe_I$) are listed alongside the sample names.

these two angular momentum vectors immediately before the collision (105°.8, Henych & Pravec 2013). The ratio of angular momentums is expressed as

$$\frac{L_T}{L_{\rm orb}} = \frac{2\pi R_T^4}{R_I^3 v_{\rm imp} P_T} \tag{9}$$

where $v_{\rm imp}$ is the velocity of the impactor (5 km s^{-1}) and P_T is the rotation period of the target (nominally 24 hr).

We also calculated the diameter of the crater, D, we expect to have been generated during the impact as

$$D = k_d V_c^{1/3} \tag{10}$$

Table 3
I–Xe Isotopic Data

Temperature (°C)	^{132}Xe[a]	1σ	^{124}Xe/^{132}Xe	1σ	^{126}Xe/^{132}Xe	1σ	^{128}Xe/^{132}Xe	1σ	^{129}Xe/^{132}Xe	1σ	^{130}Xe/^{132}Xe	1σ	^{131}Xe/^{132}Xe	1σ	^{134}Xe/^{132}Xe	1σ	^{136}Xe/^{132}Xe	1σ
Tagish Lake chondrules			~3 mg															
538	1.568E+06	5.1E+04	0.0089	0.0048	0.0024	0.0014	0.1615	0.0099	0.9889	0.0355	0.1514	0.0090	0.8264	0.0302	0.3950	0.0167	0.3539	0.0146
795	5.948E+06	8.8E+04	0.0046	0.0014	0.0032	0.0007	0.1810	0.0038	0.9843	0.0136	0.1571	0.0032	0.8069	0.0117	0.3818	0.0063	0.3435	0.0058
842	2.020E+06	5.4E+04	0.0060	0.0030	0.0037	0.0011	0.1673	0.0081	1.0047	0.0298	0.1498	0.0063	0.7891	0.0252	0.3814	0.0138	0.3428	0.0119
894	2.049E+06	6.2E+04	0.0077	0.0039	0.0024	0.0013	0.1515	0.0086	0.9713	0.0327	0.1595	0.0072	0.7891	0.0265	0.3680	0.0153	0.2940	0.0122
940	2.076E+06	5.1E+04	−0.0029	0.0034	0.0047	0.0014	0.1707	0.0075	0.9621	0.0260	0.1551	0.0061	0.7992	0.0223	0.3745	0.0140	0.3099	0.0117
1005	3.187E+06	6.3E+04	0.0049	0.0026	0.0034	0.0009	0.1890	0.0057	1.0149	0.0209	0.1577	0.0045	0.8330	0.0179	0.3925	0.0105	0.3449	0.0089
1085	5.145E+06	7.7E+04	0.0058	0.0014	0.0045	0.0005	0.1921	0.0040	0.9929	0.0141	0.1470	0.0035	0.7984	0.0124	0.3994	0.0070	0.3478	0.0062
1140	4.723E+06	7.4E+04	0.0060	0.0016	0.0032	0.0006	0.1843	0.0042	0.9312	0.0140	0.1432	0.0035	0.7598	0.0120	0.3955	0.0078	0.3438	0.0066
1199	3.523E+06	6.3E+04	0.0049	0.0017	0.0045	0.0008	0.1943	0.0054	1.0191	0.0184	0.1580	0.0043	0.8126	0.0153	0.4011	0.0087	0.3519	0.0082
1250	4.102E+06	7.0E+04	0.0025	0.0015	0.0047	0.0008	0.1703	0.0049	1.0271	0.0173	0.1488	0.0041	0.8238	0.0144	0.4009	0.0081	0.3482	0.0076
1274	3.269E+06	6.6E+04	0.0022	0.0019	0.0023	0.0007	0.1338	0.0048	1.0405	0.0220	0.1624	0.0051	0.7917	0.0171	0.4140	0.0103	0.3586	0.0089
1336	8.782E+05	3.9E+04	−0.0039	0.0084	−0.0000	0.0027	0.1621	0.0148	1.0963	0.0553	0.1659	0.0133	0.8727	0.0475	0.4056	0.0258	0.3805	0.0232
1334	5.686E+05	3.2E+04	0.0125	0.0093	0.0040	0.0027	0.2149	0.0207	1.0650	0.0700	0.1432	0.0186	0.8267	0.0594	0.5048	0.0390	0.4018	0.0321
1400	7.750E+05	4.0E+04	0.0239	0.0070	0.0010	0.0026	0.1931	0.0171	1.0012	0.0591	0.1520	0.0138	0.8762	0.0522	0.4402	0.0302	0.3785	0.0258
1432	8.215E+05	4.6E+04	−0.0034	0.0063	0.0115	0.0025	0.2373	0.0190	1.0710	0.0695	0.1787	0.0156	0.8374	0.0541	0.4242	0.0272	0.3999	0.0283
1431	1.034E+06	3.9E+04	0.0060	0.0055	0.0005	0.0021	0.1940	0.0139	1.0690	0.0450	0.1578	0.0095	0.8978	0.0405	0.4430	0.0241	0.4168	0.0205
1464	1.028E+06	4.2E+04	0.0185	0.0058	−0.0017	0.0023	0.1588	0.0138	0.9656	0.0449	0.1638	0.0126	0.8252	0.0415	0.4517	0.0258	0.3980	0.0217
>1500	1.074E+06	4.5E+04	0.0154	0.0069	0.0052	0.0018	0.2038	0.0146	0.9659	0.0462	0.1569	0.0116	0.8234	0.0435	0.4110	0.0233	0.3752	0.0212
Tagish Lake magnetite separate			~13 mg															
537	1.092E+08	1.1E+06	0.0032	0.0001	0.0037	0.0001	1.1020	0.0050	0.9687	0.0043	0.1525	0.0010	0.7970	0.0037	0.3833	0.0019	0.3255	0.0017
796	4.306E+07	5.5E+05	0.0054	0.0005	0.0042	0.0003	0.8437	0.0098	1.0316	0.0109	0.1608	0.0024	0.6454	0.0067	0.3811	0.0048	0.3254	0.0043
844	5.373E+07	5.6E+05	0.0058	0.0003	0.0042	0.0002	0.1164	0.0012	1.0316	0.0067	0.1607	0.0015	0.8376	0.0055	0.3825	0.0031	0.3284	0.0026
897	5.845E+07	5.5E+05	0.0047	0.0001	0.0039	0.0001	0.1028	0.0008	1.0276	0.0041	0.1634	0.0009	0.8252	0.0034	0.3796	0.0018	0.3280	0.0016
943	6.098E+07	5.8E+05	0.0051	0.0002	0.0038	0.0001	0.0940	0.0007	1.0269	0.0041	0.1644	0.0009	0.8216	0.0033	0.3782	0.0018	0.3261	0.0017
996	6.662E+07	6.3E+05	0.0041	0.0001	0.0042	0.0001	0.0888	0.0006	1.0300	0.0039	0.1640	0.0009	0.8113	0.0031	0.3771	0.0018	0.3227	0.0015
1102	6.042E+07	5.7E+05	0.0040	0.0002	0.0046	0.0001	0.0864	0.0006	1.0393	0.0039	0.1632	0.0009	0.8231	0.0033	0.3815	0.0018	0.3255	0.0015
1145	5.125E+07	4.9E+05	0.0043	0.0002	0.0041	0.0002	0.0841	0.0006	1.0312	0.0046	0.1598	0.0011	0.8169	0.0037	0.3774	0.0020	0.3149	0.0017
1199	5.345E+07	5.1E+05	0.0043	0.0002	0.0044	0.0001	0.0862	0.0006	1.0341	0.0042	0.1615	0.0010	0.8230	0.0035	0.3704	0.0020	0.3157	0.0016
1245	6.239E+07	5.9E+05	0.0044	0.0002	0.0043	0.0001	0.0839	0.0007	1.0265	0.0043	0.1640	0.0009	0.8187	0.0034	0.3705	0.0018	0.3199	0.0016
1298	8.835E+07	8.2E+05	0.0045	0.0001	0.0041	0.0001	0.0849	0.0005	1.0345	0.0035	0.1626	0.0008	0.8168	0.0028	0.3711	0.0015	0.3148	0.0013
1321	8.536E+07	8.0E+05	0.0045	0.0001	0.0043	0.0001	0.0850	0.0005	1.0388	0.0038	0.1634	0.0008	0.8207	0.0029	0.3731	0.0015	0.3140	0.0013
1373	3.812E+07	3.8E+05	0.0043	0.0002	0.0041	0.0002	0.0850	0.0008	1.0300	0.0054	0.1637	0.0012	0.8230	0.0044	0.3750	0.0023	0.3159	0.0019
1410	2.203E+07	2.3E+05	0.0053	0.0004	0.0041	0.0002	0.0840	0.0010	1.0480	0.0069	0.1658	0.0016	0.8256	0.0058	0.3748	0.0031	0.3162	0.0026
1448	1.483E+07	1.7E+05	0.0059	0.0005	0.0043	0.0002	0.0823	0.0014	1.0231	0.0087	0.1612	0.0020	0.8139	0.0072	0.3717	0.0045	0.3161	0.0036
1480	7.700E+06	1.0E+05	0.0044	0.0010	0.0044	0.0004	0.0888	0.0021	1.0381	0.0118	0.1648	0.0029	0.8254	0.0099	0.3754	0.0052	0.3212	0.0046
>1500	5.498E+06	8.4E+04	0.0068	0.0012	0.0048	0.0005	0.0905	0.0024	1.0333	0.0150	0.1630	0.0038	0.8219	0.0127	0.3591	0.0056	0.3198	0.0060
Tagish Lake olivine/enstatite			~5 mg															
539	4.888E+07	4.7E+05	0.0031	0.0001	0.0032	0.0001	0.1260	0.0008	0.9784	0.0042	0.1530	0.0010	0.7950	0.0034	0.3857	0.0020	0.3301	0.0018
802	1.560E+07	1.7E+05	0.0023	0.0005	0.0031	0.0002	0.1151	0.0015	0.9683	0.0075	0.1506	0.0017	0.8045	0.0069	0.3928	0.0039	0.3377	0.0030

Table 3
(Continued)

Temperature (°C)	^{132}Xe[a]	1σ	^{124}Xe/^{132}Xe	1σ	^{126}Xe/^{132}Xe	1σ	^{128}Xe/^{132}Xe	1σ	^{129}Xe/^{132}Xe	1σ	^{130}Xe/^{132}Xe	1σ	^{131}Xe/^{132}Xe	1σ	^{134}Xe/^{132}Xe	1σ	^{136}Xe/^{132}Xe	1σ
889	1.018E+07	1.2E+05	0.0037	0.0008	0.0033	0.0002	0.1221	0.0022	0.9892	0.0099	0.1493	0.0022	0.7983	0.0084	0.3956	0.0048	0.3443	0.0042
1004	3.185E+06	7.4E+04	0.0048	0.0027	0.0020	0.0006	0.2074	0.0065	0.9794	0.0246	0.1453	0.0051	0.8495	0.0220	0.4151	0.0122	0.3472	0.0098
1089	4.401E+06	7.8E+04	0.0058	0.0016	0.0039	0.0007	0.2278	0.0053	0.9794	0.0176	0.1498	0.0042	0.8188	0.0157	0.4076	0.0090	0.3672	0.0080
1148	4.161E+06	7.5E+04	0.0044	0.0019	0.0034	0.0007	0.2448	0.0055	0.9256	0.0171	0.1366	0.0040	0.8554	0.0160	0.4176	0.0090	0.3977	0.0089
1192	3.104E+06	6.6E+04	0.0033	0.0020	0.0027	0.0008	0.2448	0.0067	0.9865	0.0220	0.1518	0.0055	0.8183	0.0185	0.4350	0.0109	0.4286	0.0108
1246	3.456E+06	7.3E+04	0.0062	0.0017	0.0037	0.0006	0.2610	0.0066	0.9230	0.0206	0.1465	0.0047	0.8430	0.0182	0.3960	0.0098	0.3853	0.0093
1291	2.098E+06	6.1E+04	0.0018	0.0027	0.0026	0.0009	0.4007	0.0138	0.9935	0.0316	0.1459	0.0069	0.8742	0.0281	0.4358	0.0148	0.3740	0.0140
1325	2.019E+06	6.3E+04	0.0066	0.0028	0.0039	0.0010	1.1571	0.0366	0.9666	0.0343	0.1426	0.0071	0.9192	0.0316	0.3837	0.0135	0.3533	0.0122
1333	1.622E+06	5.5E+04	0.0136	0.0046	0.0058	0.0017	0.9823	0.0350	0.8871	0.0340	0.1388	0.0089	0.8410	0.0315	0.4434	0.0184	0.4162	0.0167
1397	1.405E+06	4.9E+04	0.0061	0.0050	0.0072	0.0013	1.4359	0.0511	0.9290	0.0369	0.1497	0.0099	0.8559	0.0348	0.4242	0.0193	0.4130	0.0181
1429	1.410E+06	4.8E+04	0.0024	0.0041	0.0073	0.0013	1.7226	0.0589	1.0093	0.0392	0.1450	0.0082	0.9592	0.0375	0.5092	0.0206	0.4636	0.0189
1434	1.643E+06	5.7E+04	0.0043	0.0049	0.0010	0.0017	2.0617	0.0709	0.9249	0.0366	0.1459	0.0067	1.0283	0.0391	0.5220	0.0212	0.5103	0.0203
1477	1.673E+06	5.5E+04	0.0119	0.0035	−0.0007	0.0015	2.3139	0.0752	0.8516	0.0311	0.1294	0.0073	1.0031	0.0350	0.5503	0.0209	0.5184	0.0191
>1500	2.037E+06	5.5E+04	−0.0005	0.0036	0.0024	0.0014	2.3092	0.0606	0.8632	0.0253	0.1347	0.0065	1.0890	0.0322	0.4812	0.0161	0.5361	0.0167
	Shallowater enstatite		∼19 mg															
538	3.767E+06	9.3E+04	0.0078	0.0021	0.0033	0.0010	4.9926	0.1176	0.9643	0.0258	0.1443	0.0075	1.1869	0.0319	0.5383	0.0161	0.5880	0.0161
795	6.942E+05	6.4E+04	0.1681	0.0199	0.0277	0.0109	4.4432	0.4133	1.1016	0.1185	0.4356	0.0521	2.1162	0.2060	0.4823	0.0560	0.5275	0.0584
897	5.783E+05	3.9E+04	0.0003	0.0087	−0.0016	0.0036	3.5371	0.2398	1.0969	0.0850	0.1446	0.0154	1.6244	0.1136	0.4116	0.0411	0.4970	0.0417
992	1.244E+06	3.6E+04	−0.0000	0.0042	0.0059	0.0015	0.8044	0.0248	1.0779	0.0339	0.1550	0.0078	1.2761	0.0386	0.4143	0.0158	0.3648	0.0139
1102	1.627E+06	4.9E+04	−0.0004	0.0022	0.0055	0.0012	0.5147	0.0180	1.0688	0.0359	0.1488	0.0078	1.9052	0.0593	0.3798	0.0134	0.3558	0.0144
1151	2.323E+06	6.2E+04	0.0017	0.0021	0.0040	0.0009	0.3233	0.0115	1.0910	0.0317	0.1534	0.0077	1.7556	0.0478	0.3914	0.0149	0.3424	0.0123
1199	2.416E+06	5.4E+04	0.0067	0.0020	0.0046	0.0009	0.2545	0.0079	1.0729	0.0258	0.1550	0.0067	1.4618	0.0335	0.3940	0.0123	0.3451	0.0105
1249	2.309E+06	5.1E+04	0.0028	0.0022	0.0053	0.0010	0.4287	0.0115	1.2718	0.0294	0.1592	0.0056	2.1782	0.0476	0.4171	0.0125	0.4384	0.0125
1293	2.421E+06	4.2E+04	0.0059	0.0021	0.0057	0.0011	4.6126	0.0722	5.5305	0.0863	0.1581	0.0062	2.4051	0.0404	0.4690	0.0124	0.4393	0.0109
1330	7.065E+06	7.9E+04	0.0051	0.0009	0.0049	0.0005	7.8214	0.0561	8.9186	0.0629	0.1564	0.0028	1.2349	0.0112	0.4097	0.0049	0.3653	0.0043
1374	5.733E+06	7.3E+04	0.0066	0.0008	0.0053	0.0004	1.0643	0.0119	1.9833	0.0206	0.1517	0.0030	1.1633	0.0131	0.4176	0.0058	0.3893	0.0052
1406	1.529E+07	1.6E+05	0.0036	0.0005	0.0034	0.0002	0.3301	0.0030	1.2628	0.0091	0.1623	0.0019	0.9513	0.0076	0.4255	0.0039	0.3969	0.0036
1443	1.658E+07	1.8E+05	0.0035	0.0003	0.0042	0.0002	0.2297	0.0024	1.1761	0.0085	0.1603	0.0017	0.8308	0.0062	0.4197	0.0037	0.3869	0.0033
1483	1.176E+07	1.4E+05	0.0056	0.0008	0.0038	0.0002	0.1938	0.0026	1.1293	0.0104	0.1597	0.0023	0.8081	0.0080	0.3952	0.0043	0.3495	0.0041
1493	5.824E+06	8.5E+04	0.0067	0.0010	0.0054	0.0004	0.2248	0.0041	1.1418	0.0154	0.1593	0.0035	0.8288	0.0121	0.3865	0.0065	0.3541	0.0060
>1500	6.574E+06	9.3E+04	0.0024	0.0012	0.0040	0.0004	0.2097	0.0036	1.1307	0.0147	0.1499	0.0024	0.8259	0.0112	0.4012	0.0063	0.3866	0.0058

Note.
[a] Isotopic abundances are reported in atoms. Heating durations are 60 s.

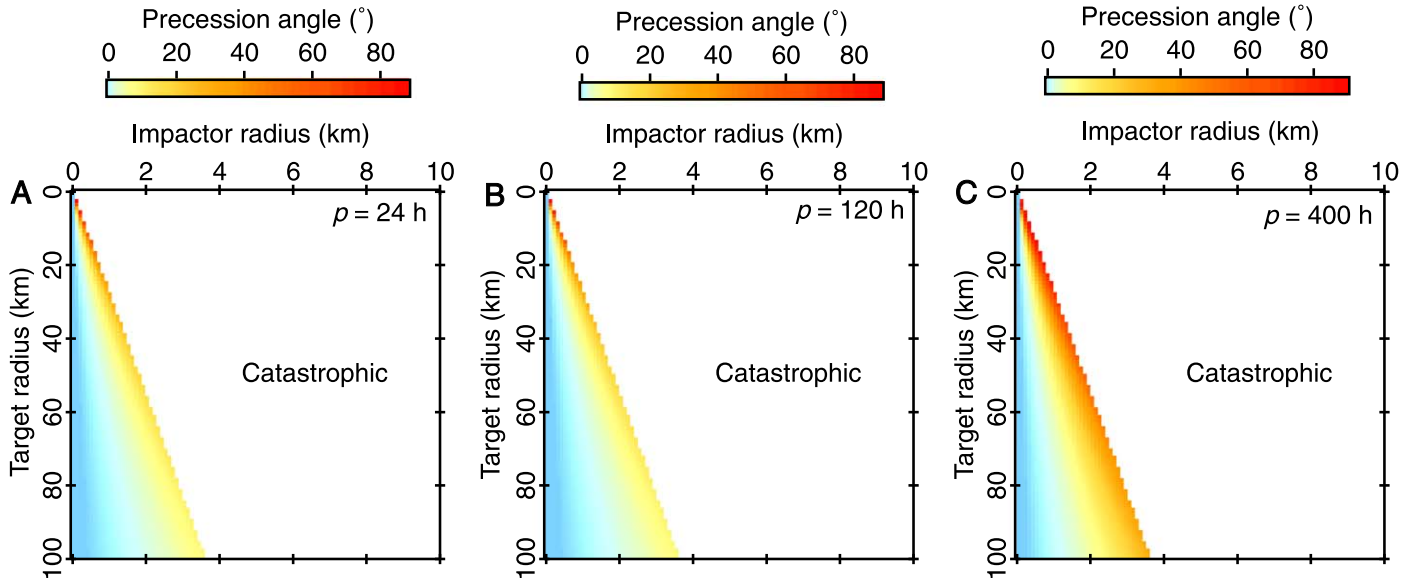

Figure 14. Calculated precession angle following an impact between two bodies with a range of radii for target body rotation periods (p) of (A) 24 hr, (B) 120 hr, and (C) 400 hr (Henych & Pravec 2013). Collisions that cause the catastrophic destruction of the target are depicted as white (Leliwa-Kopystynski et al. 2008). Impacts that are noncatastrophic are colored according to the calculated precession angle depicted by the color bars. The vast majority of impact and target radii combinations produce precession angles $\ll 15^\circ$ for $p = 24$ hr and the small fraction of collisions that do produce precession angles $>15^\circ$ involve small (<10 km) target bodies. Wider ranges of impactor and target radii cause high precession angles for longer target body rotation periods.

where

$$V_c = \frac{32\pi}{3} R_I^3 \frac{\delta}{\rho} \pi_V \tag{11}$$

$$\pi_V = K_1 \left\{ \pi_2 \left(\frac{\rho}{\delta} \right)^{(6\upsilon-2-\mu)/3\mu} + K_2 \left[\pi_3 \left(\frac{\rho}{\delta} \right)^{(6\upsilon-2)/3\mu} \right]^{(2+\mu)/2} \right\}^{-3\mu/(2+\mu)} \tag{12}$$

$$\pi_2 = \frac{2gR_I}{U^2} \tag{13}$$

$$\pi_3 = \frac{\bar{Y}}{\rho U^2} \tag{14}$$

where K_d is a shape constant (which for rocky material is 0.6), δ and ρ are the impactor and target densities (both taken as 2000 kg m^{-3}), K_1, K_2, υ, and μ are values taken from laboratory impact experiments performed on rocky material (0.095, 0.257, 0.33, and 0.55, respectively), g is the gravitational acceleration at the point of impact, U is the impact velocity component perpendicular to the local surface for an assumed impact angle of 15°, and $\bar{Y}$ is the material strength of the target (10 MPa for rocky material). Impacts that produce $D/R_T > 1.6$ are generally accepted to have caused the catastrophic destruction of the target body (Leliwa-Kopystynski et al. 2008).

We find that for impacts that did not catastrophically destroy the target body, values of θ are $<15^\circ$ (the range of angles for which precession cannot be identified from asteroid light curves) for 99.8% of our radius combinations (Figure 14) (Henych & Pravec 2013). For the very few radius combinations that produce $\theta > 15^\circ$, R_T is <10 km and the impactor radius has to be just below the critical size that would cause the target body to be catastrophically destroyed. It is possible to increase the proportion of radius combinations that produce $\theta > 15^\circ$ by increasing the rotation period. Increasing the period to 120 hr results in $\theta < 15^\circ$ for 94.5% of radius combinations we examined (Figure 14(B)) and increasing the rotation period to 400 hr results in $\theta < 15^\circ$ for 68.0% of radius combinations we examined (Figure 14(C)). Therefore, small bodies that are slowly rotating are more likely to precess if they happened to be impacted by a body with precisely the right radius. The radius of the Tagish Lake parent body must have been $\gtrsim$10 km to retain sufficient radiogenic heat to cause the extensive aqueous alteration observed in Tagish Lake (Doyle et al. 2015), making it unlikely that the Tagish Lake parent body would precess following an impact. It is also very unlikely that the rotational period of the Tagish Lake parent body was long based simply on the very small fraction of asteroid-sized bodies with long periods at the present day (only 3.2% and 0.6% of bodies that have had their rotation periods measured have periods >120 hr and >400 hr, respectively, from the JPL/NASA small-body database). It is therefore very unlikely that the Tagish Lake parent body had the necessary properties to allow it to precess even if it did happen to be impacted by a body with precisely the necessary radius. Coupled with internal dissipation, these results demonstrate that it is extremely unlikely that the weak remanence measured in Tagish Lake is the result of parent body precession.

It is also possible that asteroids could have precessed during accretion as they gained mass. For a typical asteroid-sized body, we also expect the damping time of this precession to be on the order of several thousand years (Pravec et al. 2014). As such, asteroids could have precessed as they grew, and this precession was then likely lost within $\sim$10 kyr of the end of accretion. A number of CM chondrites show evidence that they originate from the regolith of their parent asteroid (e.g., Jenniskens et al. 2012), suggesting that this material was some of the last to be added to this body. These meteorites will then have started to experience aqueous alteration once they reached the temperature at which ice melted, which typically occurred

several hundred thousand years after the start of accretion (assuming near-instantaneous accretion at ~3–4 Myr after CAI formation; Fujiya et al. 2012; Doyle et al. 2015; Bryson et al. 2019). As such, we anticipate that aqueous alteration and magnetite formation occurred once precession due to growth had likely been damped. This conclusion is consistent with the unidirectional magnetic remanence recorded by the CM chondrites (Cournede et al. 2015), which indicates that the orientation of these meteorites did not vary with respect to the field that imparted their remanence as this remanence was recorded. We expect a similar accretional and aqueous history for Tagish Lake and, as such, do not expect that precession due to parent body growth is the reason behind the weak remanence carried by this meteorite.

4.3. The Effect of the Verwey Transition on the Recovered Paleointensity

Magnetite undergoes a cubic to monoclinic phase transition on cooling through ~125 K, known as the Verwey transition (Verwey 1939). The surface of the Tagish Lake parent body could have cooled below the Verwey transition temperature if it spent a long time at large heliocentric distances ($\gtrsim$ 5 au, Weiss et al. 2010). This transition causes the magnetocrystalline anisotropy of magnetite to increase by a factor of 15 and the symmetry of this anisotropy to change dramatically (Bryson et al. 2013), which will have affected the remanence carried by Tagish Lake. However, this transition only affects the remanence carried by low-coercivity grains, leaving the remanence carried by high-coercivity grains unaffected (Dunlop & Argyle 1991). We attempted to measure the effect of the Verwey transition on an ARM carried by Tagish Lake, but the very friable nature of this meteorite meant that our test subsample crumbled during handling. Previous measurements of the more physically robust Kaba CV meteorite (Gattacceca et al. 2016), which also possesses an NRM carried by magnetite, have found that cycling through the Verwey transition has a very weak effect on the remanence carried by grains with coercivities <10 mT and no effect on the remanence carried by grains with coercivities >10 mT or the recovered HC paleointensities. As the pre-terrestrial magnetization in Tagish Lake is carried by HC grains in our subsamples, we do not expect that the Verwey transition had a detrimental effect on the paleointensity we recovered from our subsamples.

Nevertheless, we attempted to calculate the effect that the Verwey transition would likely have had on the ARMs we imparted to Tagish Lake by passing the ARM demagnetizations curves measured from our high-fidelity subsamples through a filter that approximates the effects of the Verwey transition (Figure 15(A)). This filter decreases the ARM remaining by different factors as a function of AF intensity, varying from a factor of 0.5 at 0 mT up to a factor of 1 (i.e., no reduction) at $\geqslant$ 40 mT. The values of this factor and the range of coercivities affected by the Verwey transition were taken from laboratory measurements of magnetite grains with sizes larger than the crystals in the magnetite framboids in Tagish Lake that had their AF demagnetization curves measured before and after cycling through the Verwey transition (Dunlop & Argyle 1991). The AF range that is affected by the Verwey transition in these controlled samples appears to extend to higher values than that in magnetite-bearing meteorite samples (Gattacceca et al. 2016). This filter reduces the intensity of the ARM at low coercivity while leaving the intensity of the ARM at high coercivity unaffected, increasing the difference between the ARM lost at low and high coercivities. Normalizing our filtered curves to their values at the LC–HC transition increased the normalized value of the HC ARM lost compared to the unfiltered curves (compare Figure 15(B) to Figure 9(A) and Figure 15(C) to Figure 9(B)). Accounting for the likely effect of the Verwey transition, therefore, strengthens our conclusions that the NRM in Tagish Lake was acquired in a field with an intensity <0.15 μT by increasing the difference between the demagnetization curves of the ARMs and the NRM.

4.4. The Formation Distance of the Tagish Lake Parent Body

The intensity of the stable component of the nebula field at the formation distance of the Tagish Lake parent body was likely <0.3 μT. This value can be used to constrain the formation distance of the Tagish Lake parent asteroid by comparing it to profiles of the intensity of this component of the nebula field with distance from the Sun predicted by MHD models (Bai & Goodman 2009; Bai 2015). These models are currently capable of predicting a relatively uncertain estimate of the intensity of this component that is the average of a number of simulations with differing parameters. However, this average does provide the functional form of the intensity of this component with distance from the Sun ($B_{\rm neb} \propto x^{-\frac{13}{8}}$, where $B_{\rm neb}$ is the intensity of the stable component of the nebula field and x is heliocentric distance), and it is possible to constrain the intensity of this profile using the paleointensities measured from meteorites that formed within the nebula lifetime. Importantly, the paleointensity recorded by a meteorite depends on the mechanism by which its NRM was acquired. Also, the intensity of the nebula field could have varied over time before it decayed completely when the nebula dissipated. As such, depending on the meteorite used, different constrained intensity profiles can be produced that each represent the paleointensity that would be recorded by different remanence acquisition mechanisms and at different times. Because Tagish Lake recorded a CRM at ~3–4 Myr after CAI formation, an estimate on the formation distance of its parent body should be recovered from an intensity profile that is constrained by paleointensities that were recorded through the same process and at the same time. Therefore, we chose to constrain this profile using the remanence carried by the CM chondrites (Cournede et al. 2015) which, as argued in Sections 1 and 4.1, is very likely a CRM imparted by the stable component of the nebula field at ~3–4 Myr after CAI formation. Accounting for the average effect of a tilted rotation axis of the CM parent body (see Section 4.2), paleomagnetic measurements of these meteorites indicate that the paleointensity recorded by CRM acquisition at ~3–4 Myr after CAI formation at the likely formation location of the CM parent body (likely 3.5–4.0 au; Desch et al. 2018) was 4 $\pm$ 3 μT (Cournede et al. 2015). For a ratio of gas to magnetic pressure $\beta = 10^4$, MHD models of the time-averaged component of the nebula field (Bai 2015) predict intensities that are within the uncertainty of this value at this likely formation distance (Figure 16). This value of β also readily achieves a solar accretion rates of $1 \times 10^{-8}\ M_{\rm Sun}\ {\rm yr}^{-1}$ (Bai 2015), which is the approximate average measured accretion rate of other Sun-like stars (Hartmann et al. 1998).

For the purposes of this study, we therefore assume that the predicted stable field intensity profile calculated using $\beta = 10^4$ represents the paleointensity that would be recorded through

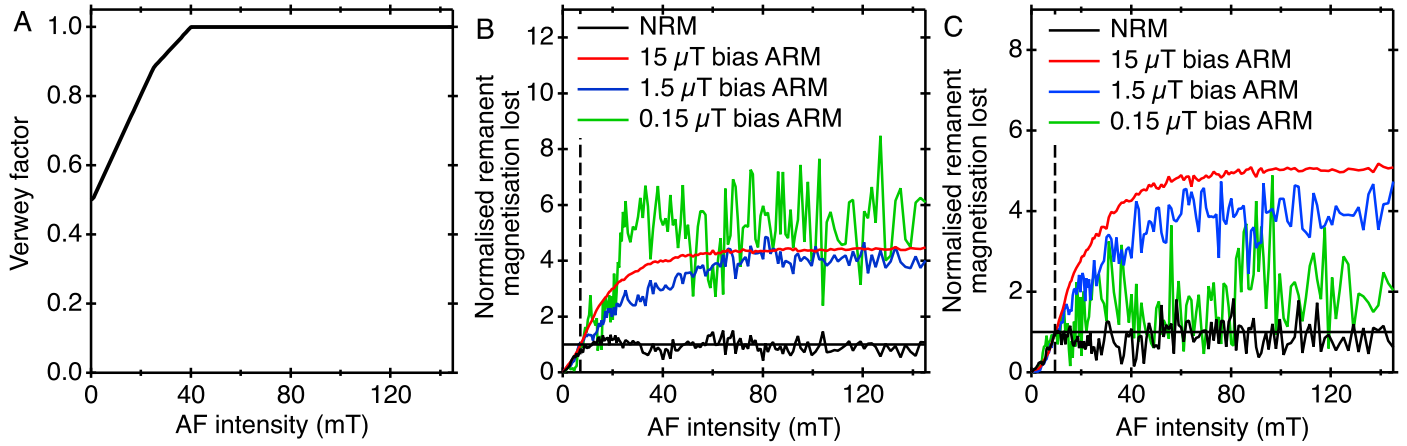

Figure 15. (A) Filter used to approximate the effect of passing magnetite-bearing samples through the Verwey transition (Dunlop & Argyle 1991). Re-calculated normalized ARM demagnetization curves for (B) TL10-4 and (C) TL10a-8a having passed the measured ARM demagnetization curves (Figure 9) through the filter in (A). Because the filter decreases the values at low coercivity while leaving those at high coercivity unaffected, the HC values of the normalized filtered ARM demagnetization curves are increased relative to the unfiltered curves and that of the NRM (compare the values of the normalized ARMs lost to those in Figure 9), strengthening our argument that the NRM was imparted in a field <0.15 μT.

CRM acquisition in the presence of the nebula field at ~3–4 Myr after CAI formation. We acknowledge that this profile remains uncertain, is model dependent, and can change considerably with different parameter values, and that our conclusions will change if future data (e.g., Borlina et al. 2019; Fu et al. 2019) are collected that support different intensity profiles. However, our choice of profile is currently justified by both the measured paleointensity of the CM chondrites and the measured accretion rate of other Sun-like stars.

The constrained profile of the stable component of the nebula field reaches intensities of <0.3 μT at distances >13 au (Figure 16). This result indicates that the Tagish Lake parent body formed in the far reaches of the solar system, possibly beyond the formation distances of the giant planets (Walsh et al. 2011). Including an additional factor of 2 onto the recovered paleointensity limit to account for possible uncertainties in the CRM/TRM value (i.e., Tagish Lake experienced a background nebula field intensity of <0.6 μT; see Section 2.4), produces a formation distance of >8 au. This distance is still significantly more distal than most other meteorite parent bodies are thought to have accreted (Desch et al. 2018) and was possibly still beyond the formation distances of Jupiter and Saturn.

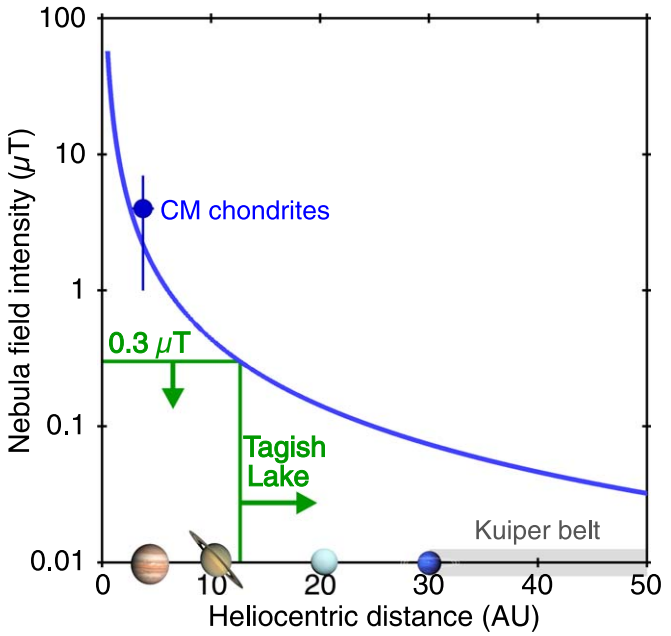

Figure 16. Recovery of the formation distance of the Tagish Lake parent body. The blue line shows the constrained intensity of the stable component of the ancient field supported by our nebula for a ratio of gas to magnetic pressure $\beta = 10^4$, which corresponds to a solar accession rate of $\sim 1 \times 10^{-8}\ M_{\rm Sun}\ {\rm yr}^{-1}$ (Bai 2015). The average paleointensity recovered from bulk CM chondrites (Cournede et al. 2015) are plotted at their hypothesized formation distances (Desch et al. 2018). This paleointensity is consistent with the calculated intensity of the stable field at this distance. Our recovered paleointensity from Tagish Lake (<0.3 μT) and corresponding range of likely formation distances (>13 au) are marked by green lines and arrows. The present-day semimajor axes of the giant planets and Kuiper Belt are included.

4.5. Constraints on Planetary Migrations

The pre-impact orbit of the Tagish Lake bolide (recovered from its well-documented fall) demonstrates that Tagish Lake came to Earth from the asteroid belt (Hildebrand et al. 2006; Granvik & Brown 2018). Combined with our recovered formation distance, these observations indicate that the Tagish Lake parent body previously migrated from the far reaches of the solar system to ~2–3 au. This motion is consistent with the predictions of models of the growth and migration of the giant planets (Gomes et al. 2005; Levison et al. 2009; Walsh et al. 2011; DeMeo & Carry 2014; Raymond & Izidoro 2017). Our results, therefore, support the ancient scattering of distal, water-rich small bodies into the inner solar system and suggest that the giant planets played a role in establishing the large-scale architecture of the solar system and populating the asteroid belt (Raymond & Izidoro 2017). These models also predict that many of the bodies that formed at $\gtrsim$10 au now constitute a significant fraction of the Kuiper Belt (~30–50 au) (DeMeo & Carry 2014). This orbital evolution implies that some Kuiper Belt objects likely formed from the same reservoir as the Tagish Lake parent body, suggesting the petrology and chemistry of these objects could be similar to those of Tagish Lake. This is most likely the case for some larger (radius $\gtrsim$10 km) Kuiper Belt objects that could have retained sufficient radiogenic heat to have undergone extensive aqueous alteration (Doyle et al. 2015).

4.6. Constraints on CAI and Chondrule Migration

Tagish Lake contains rare CAIs, most of which are ~200–300 μm in diameter and the largest of which are ~2000 μm in diameter (Zolensky et al. 2002). It also contains sparse chondrules, most of which are 250–1000 μm in diameter (Zolensky et al. 2002) and the largest of which are ~3000 μm in diameter (Russell et al. 2010). Combined with our constraint on the formation distance and likely accretion age of the Tagish Lake parent body, this observation indicates that CAIs and chondrules with a range of sizes up to a few millimeters were present in the far reaches of the solar system within ~3–4 My of the formation of CAIs. The abundance of CAIs in Tagish Lake has not been numerically constrained. However, descriptions of this meteorite (Zolensky et al. 2002; Greshake et al. 2005; Blinova et al. 2014b) suggest they are likely more abundant than CAIs in the ordinary chondrites (i.e., $\gtrsim$0.1 vol%) and possibly have an abundance similar to the CR chondrites (i.e., ~0.5 vol%; Desch et al. 2018). This observation indicates that a relatively high abundance of millimeter-sized solids traveled efficiently from the innermost solar system to the far reaches of the solar system in just a few million years with an average speed $\gtrsim$3 au Myr^{-1}(for a formation distance of the Tagish Lake parent body of >13 au).

The chondrules in Tagish Lake have not been dated, but chondrules in other carbonaceous chondrite groups formed between ~2.5–5.0 My after CAI formation (Budde et al. 2016; Schrader et al. 2017). Assuming chondrules in Tagish Lake formed at the oldest possible age within this range and at a similar location in the nebula (~3–4 au; Desch et al. 2018), these solids appear to have migrated at $\gtrsim$ 6 au Myr^{-1}(for a formation distance of the Tagish Lake parent body of >13 au), which is slightly faster than current model predictions of gas and dust motion (~4 au Myr^{-1}; Desch et al. 2018). We suggest that either chondrules in Tagish Lake are older than those in other carbonaceous chondrites (so they could have made it to the far reaches of the solar system within the likely accretion age of the Tagish Lake parent body for current predicted gas and dust migration speed (Desch et al. 2018) or that some millimeter-sized objects were able to travel particularly efficiently throughout the protoplanetary disk. Together, these observations provide new constraints on the maximum distances and speeds of millimeter-sized solid migration to the far reaches of the solar system as well as the size and abundance of these objects at large heliocentric distances.

Fragments of CAIs and chondrules have also been observed in the material collected from the coma of comet 81P/Wild 2 by the *Stardust* mission (Brownlee et al. 2006) with similar abundance (~0.5 vol%; Joswiak et al. 2017) to those possibly observed in Tagish Lake. This observation also indicates that CAIs and chondrules were present in the far reaches of the solar system. The process by which these solids were incorporated into this distal reservoir of dust and gas from which 81P/Wild 2 accreted is a subject of active research and they could have had a similar preaccretionary history to those in Tagish Lake.

5. Conclusions

1. Orbital evolution models hypothesize that large numbers of asteroid-sized bodies could have been scattered throughout the solar system over short time periods following gravitational interactions with migrating/growing giant planets. Despite the central role these events could have played in populating the asteroid belt, delivering water-rich bodies to the inner solar system and establishing the large-scale architecture of the solar system, the existence, let alone quantitative constraints on the timing and distances, of this small-body motion is poorly constrained by observations from the meteorite record. This is due in part to difficulties in recovering the formation distances and orbital evolutions of meteorite parent bodies from laboratory measurements.
2. The oldest millimeter-sized solids (CAIs and chondrules) have also been proposed to have migrated throughout the solar system, which is thought to have been key to their survival. However, our understanding of the mechanisms driving this motion as well as its timings and distances are also limited due to the lack of constraints on the formation distances of meteorite parent bodies.
3. With the aim of constraining the formation distance of a meteorite parent body, we measured the NRM carried by the Tagish Lake meteorite. This meteorite underwent aqueous alteration on its parent asteroid, during which it recorded a CRM. This process very likely occurred within the lifetime of the solar nebula, such that this meteorite potentially recorded a remanence of the magnetic field supported by the nebula. We find that Tagish Lake does not carry a resolvable HC remanence, which indicates that it experienced an ancient field intensity <0.15 μT. Accounting for the average effect of a tilted rotation axis, this result suggests that the TRM-equivalent intensity of the nebula field at the formation distance of the Tagish Lake parent body was most likely <0.3 μT (accounting for possible uncertainties in the CRM/TRM value, this paleointensity limit becomes <0.6 μT).
4. Using constrained MHD models of the stable component of the nebula field, this paleointensity corresponds to a likely formation distance of >13 au (>8 au accounting for possible uncertainties in the CRM/TRM value). This observation indicates that the Tagish Lake parent asteroid formed in the far reaches of the solar system, possibly beyond the formation distances of the gas giants.
5. Tagish Lake came to Earth from the asteroid belt. Combined with our recovered formation distance, this result indicates that some asteroid-sized bodies travelled large distances throughout the solar system. This observation supports the gas giants having played a key role in the large-scale architectural and chemical evolution of the solar system.
6. Tagish Lake contains CAIs and chondrules, indicating that millimeter-sized solids were present in the far reaches of the solar system by ~3–4 Myr after CAI formation. This result favors the efficient outward transport of these objects and provides constraints on their sizes and abundances at large heliocentric distances.

J.F.J.B. acknowledges St. John's College, University of Cambridge for funding. J.F.J.B. and B.P.W. thank the NASA Emerging Worlds program (grant #NNX15AH72G) and Thomas F. Peterson, Jr. for support. W.S.C.'s work was performed under the auspices of the U.S. Department of Energy by Lawrence Livermore National Laboratory under Contract DE-AC52-07NA27344 and was supported by Laboratory Directed Research and Development grant 17-ERD-001. We thank Chris Herd for loaning us the Tagish Lake sample (University of Alberta Meteorite

Collection, number MET11611/P-10a/17/4) and Richard Harrison, John Biersteker and Christie Jilly-Rehak for helpful discussions. We also thank Ian Garrick-Bethell for a constructive review. The paleomagnetic data presented in this paper can be found on the MagIC database (https://www2.earthref.org/MagIC).

ORCID iDs

James F. J. Bryson https://orcid.org/0000-0002-5675-8545

References

Alexander, C. M. O., Cody, G. D., Kebukawa, Y., et al. 2014, M&PS, 49, 503
Almeida, T. P., Kasama, T., Muxworthy, A. R., et al. 2014, NatCo, 5, 5154
Amelin, Y., Krot, A. N., Hutcheon, I. D., & Ulyanov, A. A. 2002, Sci, 297, 1678
Bai, X. N. 2015, ApJ, 798, 84
Bai, X. N., & Goodman, J. 2009, ApJ, 701, 737
Blinova, A. I., Herd, C. D. K., & Duke, M. J. M. 2014a, M&PS, 49, 1100
Blinova, A. I., Zega, T. J., Herd, C. D. K., & Stroud, R. M. 2014b, M&PS, 49, 473
Borlina, C. S., Weiss, B. P., Bryson, J. F. J., Fu, R. R., & Lima, E. A. 2019, in 50th Lunar and Planetary Science Conf. (Universities Space Research Association: Houston, TX), 2720
Brown, P. G., Hildebrand, A. R., Zolensky, M. E., et al. 2000, Sci, 290, 320
Brownlee, D., Tsou, P., Aléon, J., et al. 2006, Sci, 314, 1711
Bryson, J. F. J., Kasama, T., Dunin-Borkowski, R. E., & Harrison, R. J. 2013, PhaTr, 86, 88
Bryson, J. F. J., Neufeld, J. A., & Nimmo, F. 2019, E&PSL, 521, 68
Bryson, J. F. J., Weiss, B. P., Harrison, R. J., Herrero-Albillos, J., & Kronast, F. 2017, E&PSL, 472, 152
Budde, G., Kleine, T., Kruijer, T. S., Burkhardt, C., & Metzler, K. 2016, PNAS, 113, 2886
Budde, G., Kruijer, T. S., & Kleine, T. 2018, GeCoA, 222, 284
Burns, J. A., Safronov, V. S., & Gold, T. 1973, MNRAS, 165, 403
Busfield, A., Gilmor, J. D., Whitby, J. A., et al. 2001, M&PS, 36, A34
Carporzen, L., Weiss, B. P., Elkins-Tanton, L. T., et al. 2011, PNAS, 108, 6386
Cassata, W. S., Cohen, B. E., Mark, D. F., et al. 2018, SciA, 4, eaap8306
Chan, Q. H. S., Zolensky, M. E., Martinez, J. E., Tsuchiyama, A., & Miyake, A. 2016, AmMin, 101, 2041
Ciesla, F. 2007, Sci, 318, 613
Cournede, C., Gattacceca, J., Gounelle, M., et al. 2015, E&PSL, 410, 62
Cuzzi, J. N., Davis, S. S., & Dobrovolskis, A. R. 2003, Icar, 166, 385
DeMeo, F. E., & Carry, B. 2014, Natur, 505, 629
Desch, S. J., Kalyaan, A., & Alexander, C. M. O. 2018, ApJS, 238, 11
Doyle, P. M., Jogo, K., Nagashima, K., et al. 2015, NatCo, 6, 7444
Dunlop, D. J., & Argyle, K. S. 1991, JGR, 96, 2007
Egli, R. 2013, GPC, 110, 302
Fu, R. R., Kehayias, P., Weiss, B. P., Scharder, D. L., & Walsworth, R. L. 2019, in 50th Lunar and Planetary Science Conf. (Universities Space Research Association: Houston, TX), 2447
Fu, R. R., Weiss, B. P., Lima, E. A., et al. 2014, Sci, 346, 1089
Fujiya, W., Sugiura, N., Hotta, H., Ichimura, K., & Sano, Y. 2012, NatCo, 3, 627
Fujiya, W., Sugiura, N., Sano, Y., & Hiyagon, H. 2013, E&PSL, 362, 130
Gattacceca, J., Weiss, B. P., & Gounelle, M. 2016, E&PSL, 455, 166
Gomes, R., Levison, H. F., Tsiganis, K., & Morbidelli, A. 2005, Natur, 435, 466
Grady, M. M., Verchovsky, A. B., Franchi, I. A., Wright, I. P., & Pillinger, C. T. 2002, M&PS, 37, 713
Granvik, M., & Brown, P. 2018, Icar, 311, 271
Greshake, A., Krot, A. N., Flynn, G. J., & Keil, K. 2005, M&PS, 40, 1413
Harrison, R. J., & Feinberg, J. M. 2008, GGG, 9, Q05016
Harrison, R. J., & Lascu, I. 2014, GGG, 15, 4671
Hartmann, L., Calvert, N., Gullbring, E., & D'Alessio, P. 1998, ApJ, 495, 385
Henych, T., & Pravec, P. 2013, MNRAS, 432, 1623
Herd, C. D. K., Blinova, A. I., Simkus, D. N., et al. 2011, Sci, 332, 1304
Hildebrand, A. R., McCausland, P. J. A., Brown, P. G., et al. 2006, M&PS, 41, 407
Hiroi, T., Zolensky, M. E., & Pieters, C. M. 2001, Sci, 293, 2234
Hua, X., & Buseck, P. R. 1998, M&PS, 33, A215
Jeffery, P. M., & Anders, E. 1970, GeCoA, 34, 1175
Jenniskens, P., Fries, M. D., Yin, Q.-Z., et al. 2012, Sci, 338, 1583
Jilly-Rehak, C. E., Huss, G. R., & Nagashima, K. 2017, GeCoA, 201, 224
Joswiak, D. J., Brownlee, D. E., Nguyen, A. N., & Messenger, S. 2017, M&PS, 52, 1612
Kimura, Y., Sato, T., Nakamura, N., et al. 2013, NatCo, 4, 3649
King, A. J., Schofield, P. F., Howard, K. T., & Russell, S. S. 2015, GeCoA, 165, 148
Kirschvink, J. L. 1980, GeoJ, 62, 699
Kirschvink, J. L., Kopp, R. E., Raub, T. D., Baumgartner, C. T., & Holt, J. W. 2008, GGG, 9, Q05Y01
Krot, A. N., Hutcheon, I. D., Brearley, A. J., et al. 2006, in Meteorites and the Early Solar System II, ed. D. S. Lauretta & H. Y. McSween (Tucson, AZ: Univ. Arizona Press), 525
Kruijer, T. S., Burkhardt, C., Budde, G., & Kleine, T. 2017, PNAS, 114, 6712
Kruijer, T. S., Kleine, T., Fischer-Godde, M., Burkhardt, C., & Wieler, R. 2014, E&PSL, 403, 317
Leliwa-Kopystynski, J., Burchell, M. J., & Lowen, D. 2008, Icar, 195, 817
Levison, H. F., Bottke, W. F., Gounelle, M., et al. 2009, Natur, 460, 364
Lewis, R. S. 1975, GeCoA, 39, 417
McClelland, E. 1996, GeoJI, 126, 271
Muxworthy, A. R., & Dunlop, D. J. 2002, E&PSL, 203, 369
Nakamura, T., Noguchi, T., Zolensky, M. E., & Tanaka, M. 2003, E&PSL, 207, 83
Nakamura-Messenger, K., Messenger, S., Keller, L. P., Clemett, S. J., & Zolensky, M. E. Z 2006, Sci, 314, 1439
Nesvorny, D. 2018, ARA&A, 56, 137
Ott, U. 2002, RvMG, 47, 71
Pravdivtseva, O., Krot, A. N., & Hohenberg, C. M. 2018, GeCoA, 227, 38
Pravdivtseva, O., Meshik, A., Hohenberg, C. M., & Krot, A. N. 2017, GeCoA, 201, 320
Pravec, P., Harris, A. W., & Michałowski, T. 2002, in Asteroids III, ed. W. F. Bottke et al. (Tucson, AZ: Univ. Arizona Press), 113
Pravec, P., Scheirich, P., Durech, J., et al. 2014, Icar, 233, 48
Quirico, E., Bonal, L., Beck, P., et al. 2018, GeCoA, 241, 17
Raymond, S. N., & Izidoro, A. 2017, SciA, 3, e1701138
Roberts, A. P., Liu, Q., Rowan, C. J., et al. 2006, JGRB, 111, B12S35
Russell, S. D. J., Longstaffe, F. J., King, P. L., & Larson, T. E. 2010, GeCoA, 74, 2484
Schiller, M., Connelly, J. N., Glad, A. C., Mikouchi, T., & Bizzarro, M. 2015, E&PSL, 420, 45
Schrader, D. L., Nagashima, K., Krot, A. N., et al. 2017, GeCoA, 201, 275
Schrader, D. L., Nagashima, K., Waitukaitis, S. R., et al. 2018, GeCoA, 223, 405
Scott, E. R. D., & Krot, A. N. 2014, in Treatise on Geochemistry, ed. H. Holland & K. Turekian (2nd ed; Amsterdam: Elsevier), 65
Shah, J., Williams, W., Almeida, T. P., et al. 2018, NatCo, 9, 1173
Stephenson, A. 1993, JGR, 98, 373
Tauxe, L., & Staudigel, H. 2004, GGG, 5, Q02H06
Thirumalai, K., Singh, A., & Ramesh, R. 2011, J. Geol. Soc. India, 77, 377
Tissot, F. L. H., Dauphas, N., & Grove, T. L. 2017, GeCoA, 213, 593
Verwey, E. J. W. 1939, Natur, 44, 327
Walsh, K. J., Morbidelli, A., Raymond, S. N., O'Brien, D. P., & Mandell, A. M. 2011, Natur, 475, 206
Wang, H., Weiss, B. P., Bai, X.-N., et al. 2017, Sci, 355, 623
Weiss, B. P., Gattacceca, J., Stanley, S., Rochette, P., & Christensen, U. R. 2010, SSRv, 152, 341
Weiss, B. P., & Tikoo, S. M. 2014, Sci, 346, 1198
Zolensky, M. E., Nakamura, K., Gounelle, M., et al. 2002, M&PS, 37, 737